Lehigh University
Lehigh Preserve

Theses and Dissertations

1-1-1982

Aspects of quantitative microanalysis using energy dispersive spectrgmetry and electron energy loss spectroscopy.

Nicola Stenton

Follow this and additional works at: http://preserve.lehigh.edu/etd

Part of the Materials Science and Engineering Commons

Recommended Citation
Stenton, Nicola, "Aspects of quantitative microanalysis using energy dispersive spectrgmetry and electron energy loss spectroscopy." (1982). *Theses and Dissertations*. Paper 2318.

This Thesis is brought to you for free and open access by Lehigh Preserve. It has been accepted for inclusion in Theses and Dissertations by an authorized administrator of Lehigh Preserve. For more information, please contact preserve@lehigh.edu.

ASPECTS OF QUANTITATIVE MICROANALYSIS USING ENERGY DISPERSIVE SPECTROMETRY AND ELECTRON ENERGY LOSS SPECTROSCOPY

by

Nicola Stenton

A Thesis

Presented to the Graduate Committee

of Lehigh University

in Candidacy for the Degree of

Master of Science in

Metallurgy and Materials Engineering

Lehigh University

1982

ProQuest Number: EP76594

All rights reserved

INFORMATION TO ALL USERS
The quality of this reproduction is dependent upon the quality of the copy submitted.

In the unlikely event that the author did not send a complete manuscript
and there are missing pages, these will be noted. Also, if material had to be removed,
a note will indicate the deletion.

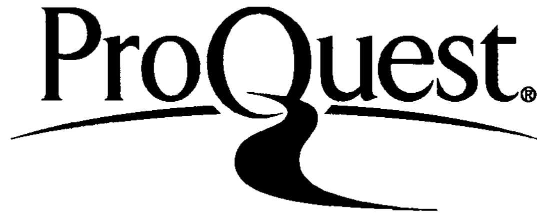

ProQuest EP76594

Published by ProQuest LLC (2015). Copyright of the Dissertation is held by the Author.

All rights reserved.
This work is protected against unauthorized copying under Title 17, United States Code
Microform Edition © ProQuest LLC.

ProQuest LLC.
789 East Eisenhower Parkway
P.O. Box 1346
Ann Arbor, MI 48106 - 1346

CERTIFICATE OF APPROVAL

This thesis is accepted and approved in partial fulfillment of the requirements for the degree of Master of Science.

July 3, 1982
(date)

Professor in Charge

Chairman of Department

ACKNOWLEDGEMENTS

I would like to express my sincere appreciation to the following people:

--My advisor, Dr. M. R. Notis for his enthusiasm and guidance throughout this work.

--Dr. D. B. Williams and Dr. J. I. Goldstein for their advice and assistance with various aspects of this work.

--Dr. D. E. Newbury of the National Bureau of Standards, Gaithersburg, MD, for the Monte Carlo calculations.

--Mr. C. Kemmerer of Bell Laboratories, Allentown, PA for preparation of the Ni films.

--Dr. W. J. Minford of Bell Laboratories, Allentown, PA for supplying the zirconia sample.

--Dave Calvert, Joe Michael and Steve Baumann for my introduction into the world of the "green screen".

--"The English Potters", Steve and Stef for teaching me the practical aspects of ceramics.

--Betty and Louise for an excellent, speedy typing job.

--DeeDee for the photographic work.

--My officemates over the past two years: Cal, Chen, Merchant, Stella and Steve for making the whole experience more enjoyable.

--The Department of Energy and Lehigh University for providing the financial support for this work.

--My parents, to whom this thesis is dedicated, for their support and encouragement throughout my life.

TABLE OF CONTENTS

		Page
	CERTIFICATE OF APPROVAL	ii
	ACKNOWLEDGMENTS	iii
	TABLE OF CONTENTS	iv
	LIST OF TABLES	vii
	LIST OF FIGURES	viii
	ABSTRACT	1
I.	INTRODUCTION	3
II.	$\phi(\rho t)$ MEASUREMENTS	7
	1. Background	7
	Experimental Measurements of (ρt) Curves	9
	Calculations of $\phi(\rho t)$ Curves	11
	2. Experimental Procedures	12
	Sample Preparation	12
	Generation of Data	14
	Considerations of Specimen Geometry	15
	Statistical Analysis	16
	3. Results and Discussion	17
III.	FOIL THICKNESS MEASUREMENTS	21
	1. Background	21
	2. Experimental Procedures	22
	3. Results and Discussion	23

TABLE OF CONTENTS (continued)

	Page
IV. ELECTRON ENERGY LOSS MEASUREMENTS	25
1. Background	25
Equipment	25
The Energy Loss Spectrum	26
Shapes of Ionization Edges	29
Detectability Limits	31
Quantitation	32
Ratio Method	34
Operating Conditions	35
Determination of Partial Ionization Cross-Sections	36
Quality of Experimental Results	38
Comparison of Energy Loss and X-ray Analysis	40
2. Experimental Procedures	42
Specimen Preparation	42
EDS Analysis	43
(i) Determination of k_{Ca-Zr}	43
(ii) Determination of Composition of $ZrO_{2(ss)}$	45
(iii) Profile across a Lamellar Interface	46

TABLE OF CONTENTS (continued)

	Page
EELS Analysis	48
(i) Energy Loss Analysis on the Philips EM400T	48
(ii) Determination of Ca/O Atomic Ratios	50
(iii) EELS Profiles	51
3. Results and Discussion	53
Microstructure of Eutectic	53
(i) $ZrO_{2(ss)}$ Phase	53
(ii) $CaZrO_3$ Phase	55
EDS Analysis	56
EELS Analysis	57
(i) Visual Comparison of Spectra	57
(ii) Evaluation of Ca/O Ratios	59
(iii) Evaluation of EELS Profiles	64
(iv) Errors in Quantitative EELS	65
V. CONCLUSIONS	67
VI. REFERENCES	125
APPENDIX I	131
APPENDIX II	134
APPENDIX III	136
VITA	138

LIST OF TABLES

No.	Title	Page
I.	Specimen Thicknesses for $\phi(\rho t)$ Determinations	69
II.	Comparison of Techniques for Thin Foil Thickness Measurements	70
III.	Variation of $\phi(\rho o)$ with Accelerating Voltage at 380 nm	71
IV.	Comparison of Thin Foil Thickness Measurements	72
V.	Relationship between Objective Aperture Diameter and Spectrometer Acceptance Angle (β)	73
VI.	Operating and Analysis Parameters used for the Evaluation of Ca/O Ratios	74
VII.	$\sigma(\beta,\Delta)$ for the Oxygen K Shell at 120 kV	75
VIII.	$\sigma(\beta,\Delta)$ for the Calcium L Shell at 120 kV	76
IX.	Operating and Analysis Parameters used for EELS Profiles	77
X.	Comparison of Experimentally Determined Ca/O Ratios under Different Analysis Conditions	78
XI.	Effect of Objective Aperture Size on Ca/O Ratio (Carbon-coated Specimens)	79
XII.	Effect of Energy Window Δ on Ca/O Ratio (Carbon-coated specimens)	80

LIST OF FIGURES

No.	Description	Page
1	Signals generated as a result of the interaction of an electron beam and a thin specimen. [From Maher and Joy[1]]	81
2	The x-ray emission volume in a thick target relative to that in a thin foil.	82
3	Sandwich sample used to measure $\phi(\rho t)$.	83
4	The $\phi(\rho t)$ curves of Castaing and Deschamps[16] measured at 29 kV.	84
5	Specimen geometry used in determination of $\phi(\rho t)$. Thicknesses of Ni varying from ~ 25 to 380 nm were deposited on top of the Cu film leaving portions exposed.	85
6a	Schematic: principles of Tolansky interferometry.	86
6b	Typical interferogram showing how L and ΔL are measured to enable specimen thickness t to be determined using equation in Figure 6a.	86
7	Schematic: measurement of thickness of deposited film of density ρ, by determining frequency shift (Δf) of quartz oscillator.	87

LIST OF FIGURES (continued)

No.	Description	Page
8	Experimental data showing increase in $\phi(\rho t)$ with mass thickness for thin films of Ni up to 380 nm thick using 120 kV electrons.	88
9	Experimental $\phi(\rho t)$ data for thin films of Ni up to 380 nm thick at 60 kV.	89
10	Comparison of experimental data from this current investigation with Monte Carlo calculations. (Work of Newbury is for Ni at 120 kV while data of Kyser is for Cu at 100 kV.)	90
11	Contamination spots created on upper and lower surfaces of evaporated Al foil.	91
12	Schematic illustration of combined electron microscope and microanalytical facility. The incident beam is focused to a spot on the thin sample and either x-ray or electron energy-loss spectra can be collected for microanalysis. [From Joy and Maher[30]]	92
13	The geometry of energy loss spectroscopy in the electron microscope, showing the scattering angle θ, the spectrometer acceptance angle β and the incident beam convergence angle α. [From Joy[32]]	93

LIST OF FIGURES (continued)

No.	Description	Page
14	Typical EELS spectra from Si at 100 kV, showing the zero loss peak, the plasmon peaks and a gain change of 50 followed by the $Si_{L_{23}}$ edge. [From Joy[32]]	94
15	Position of ionization edges in energy loss range 0-700 eV. [From Joy and Maher[34]]	95
16	Log-log plot of an energy-loss spectrum showing subtraction of background intensity. [After Egerton and Whelan[35]]	96
17	(a) Typical shape of a K ionization edge. (b) Typical shapes of L_{23} ionization edges. (c) Typical shape of an M_{45} edge. [After Menzies and Bricknell[37]]	97
18	(a) The calculated self-detection limits for an ELS system operating at 100 kV with an acceptance angle of 3 mrad. (b) Minimum detectable number of atoms for various elements in a 50 nm thick Fe foil under the same operating conditions. [From Joy and Maher[41]]	98
19	Schematic illustration of an energy loss spectrum indicating the quantities required for quantitation. [From Joy and Maher[45]]	99

LIST OF FIGURES (continued)

No.	Description	Page
20	ZrO_2-CaO phase diagram due to Stubican and Hellman (1981).[55]	100
21	Low magnification transmission optical micrograph of the $CaZO_3/ZrO_{2(ss)}$ directionally solidified eutectic.	101
22	TEM micrograph of the $CaZrO_3/ZrO_{2(ss)}$ eutectic structure.	102
23	[100] diffraction pattern from the $ZrO_{2(ss)}$ phase.	103
24	(a) and (b) Diffraction patterns from $ZrO_{2(ss)}$ phase showing diffuse "donut" shaped features.	104
25	Bright field micrograph of $ZrO_{2(ss)}$ phase showing mottled contrast associated with the diffuse diffraction features of Figure 24.	105
26	(a) and (b) Typical boundaries observed in $CaZrO_3$ phase.	106
27	Behavior of bend contours indicates presence of low angle boundaries in some areas of $CaZrO_3$ phase.	107
28	δ boundaries in $CaZrO_3$ (a) Asymmetrical fringe contrast in bright field. (b) Symmetrical fringe contrast in dark field.	108

LIST OF FIGURES (continued)

No.	Description	Page
29	Diffraction pattern from $CaZrO_3$ showing retained high temperature, ordered cubic form.	109
30	Cubic diffraction pattern from $CaZrO_3$ with no evidence of extra spots due to ordering.	110
31	Non-cubic diffraction pattern from $CaZrO_3$.	111
32	(a) Typical EDS spectrum from $CaZrO_3$ phase. (b) Typical EDS spectrum from $ZrO_{2(ss)}$ phase.	112
33	EDS profile across a lamellar interface showing no appreciable cation segregation at the boundary.	113
34	(a) Typical EELS spectrum from $CaZrO_3$ phase. (b) Typical EELS spectrum from $ZrO_{2(ss)}$ phase.	114
35	Effect of objective aperture size on spectra from $CaZrO_3$ phase. (a) Spectrum using 100 μm aperture (β = 9.73 mrads). (b) Spectrum using 50 μm aperture (β = 4.86 mrads) showing improved edge to background signal.	115
36	Effect of objective aperture size on spectra from $ZrO_{2(ss)}$ phase. (a) Using 100 μm	116

LIST OF FIGURES (continued)

No.	Description	Page
	aperture (β = 9.73 mrads). (b) Using 50 μm aperture (β = 4.86 mrads).	
37	Typical EELS spectra from Al coated specimen. (a) $CaZrO_3$ phase. (b) $ZrO_{2(ss)}$ phase.	117
38	Portion of EELS spectrum showing background fit to the oxygen K edge.	118
39	Portion of EELS spectrum from Al coated specimen showing poor fit to the calcium edge.	119
40	Portion of EELS spectrum from C coated specimen showing a reasonable fit to the calcium edge.	120
41	Portion of EELS spectrum from an evaporated Al film maintained under the same conditions as the Al coated specimen, showing a small oxygen edge.	121
42	Ca/O profiles across a lamellar interface using medium objective aperture (β=4.86 mrads) and energy windows of 20 eV and 50 eV.	122
43	Ca/O profiles across a lamellar interface using large objective aperture (β=9.73 mrad) and energy windows of 20 eV and 50 eV.	123

LIST OF FIGURES (continued)

No.	Description	Page
44	Low index diffraction pattern from Al superimposed with image of objective aperture. [Courtesy S. F. Baumann]	124

ABSTRACT

Three topics currently of interest in quantitative microanalysis, related to both energy dispersive x-ray analysis (EDS) and energy loss spectroscopy (EELS), have been investigated to assess the accuracy of the respective quantitation procedures.

Using EDS analysis, the depth of x-ray production in a thin Ni foil has been determined by comparing the x-ray intensity emitted from a Cu tracer layer covered with various thicknesses of Ni, with the intensity from the isolated tracer layer. It has generally been assumed that the depth of x-ray production does not vary with thickness in thin foils, however, this investigation indicated a 30% increase in x-ray production over a thickness range 0-380 nm. This result has important implications for systems in which x-ray absorption is significant because a knowledge of the depth of x-ray production is required to calculate an absorption correction factor.

Another parameter that is critical to the absorption correction factor is the foil thickness, which is commonly measured by the contamination spot method. The use of evaporated metallic foils, the thicknesses of which are known to $\pm$ 5 nm using Tolansky interferometry, has permitted comparison with measurements from the contamination spot technique. It was found that the contamination spot method considerably overestimated the true foil thick-

ness by a factor of between 1.5 and 3, the error being greatest for foils <100 nm thick, implying that this technique may be of limited reliability.

The accuracy of present EELS quantitation procedures has been assessed using a directionally solidified eutectic in the ZrO_2-CaO system. Previous studies using EELS have been limited to simple two-component systems. In the present study $^{Ca}/_{O}$ ratios were determined under various operating and analysis conditions and showed good agreement with values calculated from the stoichiometry. Systematic errors in the EELS data were attributed to difficulties in fitting the Ca edge, due to the proximity of other edges in the spectrum, highlighting one of the major problems associated with analysis of multicomponent systems. In addition, sharp discontinuities in the $^{Ca}/_{O}$ ratio were observed when profiling across lamellar interfaces, indicating that EELS shows good sensitivity to abrupt changes in composition and has potential for quantitative light element analysis.

I. INTRODUCTION

When a high energy electron beam interacts with a thin foil many secondary signals are produced, as indicated in Figure 1.[1] The development of the scanning transmission electron microscope (STEM) has enabled many of these signals to be detected and subsequently processed to give quantitative data, while still preserving the capability of high resolution imaging.

This work deals with quantitative analysis techniques using two of these characteristic signals, namely energy dispersive spectrometry (EDS) of x-rays and electron energy loss spectroscopy (EELS) of inelastically scattered electrons.

Quantitative x-ray analysis is now well established and is routinely performed using the STEM coupled with an energy dispersive x-ray spectrometer and multichannel analyzer. Characteristic x-rays are produced when an incident electron ejects an electron from one of the inner shells of an atom in the specimen. The atom returns to its normal energy state when one of its outer electrons falls into the inner shell and emits energy in the form of x-radiation. In thin foils x-rays are emitted uniformly in all directions but since the detector only subtends a small solid angle at the specimen only a fraction of the x-ray signal can be detected. Thus quantitation of EDS measurements cannot give absolute concentrations but relies on a ratio technique to give relative concentrations of two or more species.

In contrast, EELS is a relatively new technique which until recently has only been used for qualitative chemical analysis. EELS gives a measure of the primary inelastic scattering event of an incident electron. For elemental analysis the most important scattering process is the ionization of the inner shell of an atom which is the first step in the production of a characteristic x-ray. The energy lost by an incident electron in ionizing the inner shell electron is characteristic of the particular atom. The inelastically scattered electrons have a small angular distribution and so the total signal can effectively be collected and analyzed, in contrast to x-rays. Thus absolute quantitation should be possible using EELS, although this is still in the developmental stage.

With recent improvements in instrumentation and an increased knowledge of electron beam/specimen interactions, there is the potential to achieve even greater accuracy in quantitative analysis. In this work three topics currently of interest in this area have been investigated. In x-ray analysis, compositions are generally determined using the Cliff-Lorimer equation[2] which relates the characteristic peak intensities I_A and I_B to the actual concentration of the species in wt.%, C_A and C_B, according to the relationship:

$$\frac{C_A}{C_B} = k_{AB} \frac{I_A}{I_B} \qquad (1)$$

where k_{AB} is a constant for a given pair of elements. In systems in which significant absorption of x-rays occurs, however, a correction factor must be applied to equation (1) to account for the effects of absorption. Goldstein, et al.[3] have proposed the following modification to equation (1), where the term in large parentheses is the correction factor:

$$\frac{C_A}{C_B} = k_{AB} \frac{I_A}{I_B} \left[\frac{\int_0^t \phi_B(\rho t) \exp\left(-\frac{\mu}{\rho}\Big]^B_{SPEC} \operatorname{cosec} \alpha(\rho t)\right) dt}{\int_0^t \phi_A(\rho t) \exp\left(-\frac{\mu}{\rho}\Big]^A_{SPEC} \operatorname{cosec} \alpha(\rho t)\right) dt} \right] \quad (2)$$

where $\phi(\rho t)$ = the depth distribution of x-ray production

$\frac{\mu}{\rho}\Big]^i_{SPEC}$ = the mass absorption coefficient for x-rays from element i in the specimen

ρ = the density of the specimen

t = the specimen thickness

α = the x-ray take-off angle

When equation (2), is used, the accuracy of the calculated composition is dependent on the accuracy of the absorption correction factor. In this equation, the depth of x-ray production $\phi(\rho t)$, is generally assumed to be equal to 1 (i.e. x-rays are generated uniformly throughout a thin foil). However, there have been no experimental measurements of $\phi(\rho t)$ for thin foils at high accelerating voltages (> 50 kV) and evidence suggests

that this assumption is not necessarily a valid one. Accordingly $\phi(\rho t)$ curves have been determined for thin Ni foils at 60 kV and 120 kV to assess the accuracy of this assumption.

Another parameter affecting the absorption correction is the foil thickness t, which is generally measured by the contamination spot method.[4] A knowledge of the foil thickness is also required to determine the size of the activation volume for x-ray analysis and to obtain absolute concentrations in EELS. Although the contamination spot method is relatively simple and can be used on most materials, its accuracy has been brought into question. In this work, therefore, thin metallic foils of known thickness (to within $\pm$ 5 nm) have permitted a comparison to be made with thickness measurements made using the contamination spot method.

Finally, in the area of energy loss spectroscopy, a more general topic has been studied, namely the accuracy of quantitative data obtained from a ceramic system of known composition. Previous work in this area has been limited to model systems such as MgO and BN in which only K shell interactions have been considered and the resulting edges are well separated. In this work a more complex system, namely a directionally solidified eutectic of CaO stabilized ZrO_2 has been used to assess the accuracy of energy loss quantitation. In this system, considerable overlap of the characteristic edges occurs and both K and L edges must be used for analysis. Hence this work provides a more rigorous test of current energy loss quantitation techniques.

II. $\phi(\rho t)$ MEASUREMENTS

1. Background

In quantitative microanalysis, we are concerned with converting measured intensity ratios into chemical compositions using either empirical or theoretical methods. For thin foils it has generally been assumed that absorption and fluorescence of x-rays within the specimen can be ignored and so a simple standardless relationship, the Cliff-Lorimer equation, can be used to determine the compositions C_A and C_B of elements A and B (as described in the previous section)

Hence:

$$\frac{C_A}{C_B} = k_{AB} \frac{I_A}{I_B} \qquad \text{(Equation 1, Section I)}$$

where k_{AB} is a constant for a fixed accelerating voltage and I_A and I_B are the characteristic peak intensities above the continuum background.

Although it has generally been established that fluorescence in thin foils can indeed be neglected, evidence suggests that absorption of x-rays is often significant if the combination of film thickness and the difference in mass absorption coefficients is large enough.[5-7] In such cases, the value of k_{AB} will vary with foil thickness and may give rise to errors in excess of $\pm$ 10% in the calculated composition. Goldstein, et al.[3] introduced a correction term into the Cliff-Lorimer equation to

account for the preferential absorption of one characteristic x-ray with respect to another.

Hence, as given in the previous section and repeated here,

$$\frac{C_A}{C_B} = k_{AB}\,\frac{I_A}{I_B}\left[\frac{\int_o^t \phi_B(\rho t)\exp\left(-\frac{\mu}{\rho}\Big]^B_{SPEC}\ \operatorname{cosec}\alpha(\rho t)\right)dt}{\int_o^t \phi_A(\rho t)\exp\left(-\frac{\mu}{\rho}\Big]^A_{SPEC}\ \operatorname{cosec}\alpha(\rho t)\right)dt}\right] \quad (2)$$

where $\phi(\rho t)$ = the depth distribution of x-ray production

$\frac{\mu}{\rho}\Big]^i_{SPEC}$ = the mass absorption coefficient for x-rays from element i in the specimen

ρ = the density of the specimen

t = the specimen thickness

α = the x-ray take-off angle

The absorption correction requires a knowledge of the distribution of x-ray production with depth, $\phi(\rho t)$. $\phi(\rho t)$ is known to vary significantly with depth in bulk specimens because of the large ionization volume (Figure 2), although values have only been obtained for relatively low electron energies (<50kV). Early calculations by Konig[8] and Yakowitz and Newbury[9] however, predicted that for all electron transparent thin foils at 100 kV, $\phi(\rho t)$ is approximately equal to 1. For thin films, therefore, it has generally been assumed that the x-ray distribution remains constant throughout the foil. Thus

$\phi_A(\rho t) = \phi_B(\rho t) = 1$ and equation (2) reduces to:

$$\frac{C_A}{C_B} = k_{AB} \frac{I_A}{I_B} \frac{\left.\frac{\mu}{\rho}\right]^{A}_{SPEC} \left[1 - \exp -\left(\left.\frac{\mu}{\rho}\right]^{B}_{SPEC} \operatorname{cosec} \alpha(\rho t)\right)\right]}{\left.\frac{\mu}{\rho}\right]^{B}_{SPEC} \left[1 - \exp -\left(\left.\frac{\mu}{\rho}\right]^{A}_{SPEC} \operatorname{cosec} \alpha(\rho t)\right)\right]} \quad (3)$$

Recent work,[10] however, has indicated that in relatively thick samples in which there is a considerable amount of absorption, equation (3) is not an accurate description of the absorption correction. This may be due in part to the assumption that $\phi(\rho t)$ is constant with foil thickness.

Experimental Measurements of $\phi(\rho t)$ Curves

Experimental $\phi(\rho t)$ curves have been determined by a number of workers [11-15] using the sandwich sample technique originally proposed by Castaing and Deschamps.[16] The sandwich sample (Figure 3) consists of a thin tracer layer which is covered by successively thicker layers of the matrix element, for which the curve is determined. The tracer layer is chosen to be one greater in atomic number than the matrix layer, so that its properties with regard to x-ray excitation may be assumed identical to those of the matrix but in addition it will not be fluoresced by the matrix. The $\phi(\rho t)$ curve is then generated by measuring the x-ray intensity emitted from the tracer layer at various depths in the matrix. Figure 4 shows the $\phi(\rho t)$ curves for

Al, Cu and Au at 29 kV as determined by Castaing and Deschamps.[16] The curves start with a $\phi(\rho t)$ value larger than unity at zero depth due to the contribution from backscatter in the specimen. The x-ray distribution then begins to increase with depth as the electron trajectories become progressively diffused in the sample, which increases their path length in the tracer layer. The curve finally drops off as the number of electrons penetrating the deeper layers decreases.

Since absorption problems are more commonly associated with bulk microanalysis in the electron microprobe or SEM, all the $\phi(\rho t)$ experiments to date have been performed on bulk specimens using relatively low accelerating voltages (< 50 kV). For a thin film specimen it is necessary to measure the intensity of radiation emitted from tracer layers at known depths relative to an identical tracer layer isolated in space. However, the total thickness t of the film (including the tracer) should be held constant and a $\phi(\rho t)$ curve obtained for that thickness. Experimentally, the production of several thin films of a given thickness each containing tracer layers at various depths is very difficult. However, if the backscatter coefficient for electrons in these films is very low the effect of the material below the tracer layer on x-ray production in the tracer layer is very small. In this case, $\phi(\rho o) = 1$; that is, the x-ray emission from the tracer layer on the surface of the film will be equal to that of the

tracer layer isolated in space.

Thus the major difference between the technique employed in this work (for thin foils), and the original technique of Castaing and Deschamps[16] is that in the latter case the composite sample was always of the same thickness and the tracer layer moved to different depths within the matrix. In this work the tracer layer always formed the base layer, and different thicknesses were deposited on top of the foil.

Calculations of $\phi(\rho t)$ Curves

Several models have been proposed in which the fundamental interactions of electrons and atoms could be used to calculate $\phi(\rho t)$ curves.[17-19] However, calculations based on Monte Carlo methods have probably received the most attention since they are capable of describing x-ray production in three dimensions and are not limited to single phase materials. Monte Carlo calculations essentially simulate a large number of electron trajectories, segment by segment, based on a mean electron range for a given accelerating voltage and target. Although there are several Monte Carlo calculation methods presently in use, they all have certain common characteristics, described in greater detail by Kyser.[20] Monte Carlo calculations of $\phi(\rho t)$ for bulk specimens, at relatively low accelerating voltages, have shown good agreement with experiment and so the technique has been extended to include thin foils at high operating voltages. The major difference between a thin foil

and a bulk specimen is that very few electrons are scattered or lose significant energy before emerging from a thin film. This leads to a small fraction of backscattered electrons and a small x-ray source. Thus Monte Carlo calculations are much simplified for thin films. Using this technique Kyser[20] has predicted that, at 100 kV, there would be no variation in $\phi(\rho t)$ with depth for a 400 nm Al film, but for films of Cu and Au (of the same thickness) $\phi(\rho t)$ increases by 5% and 20% respectively.

Although it would appear that Monte Carlo calculations offer a quicker and more convenient method for generating $\phi(\rho t)$ curves there is much uncertainty as to the accuracy of the input parameters used to describe the electron interactions. Therefore to establish the reliability of these calculations for thin foils, there is a need to compare the calculations with measured curves, for a variety of elements and electron voltages.

2. Experimental Procedures

Sample Preparation

A series of thin film samples were prepared for the determination of the $\phi(\rho t)$ curve for Ni, each having an initial layer of Cu, approximately 60 nm thick acting as the tracer element. Different thicknesses of Ni were then deposited on the samples leaving a section of the tracer layer exposed on each specimen. The specimen geometry is shown in Figure 5. Both the tracer and matrix layers were prepared by vacuum

evaporation and deposition onto a 2.5 mm square single crystal of sodium chloride. The Cu was deposited by thermal evaporation from a heated tungsten filament, and the Ni by electron beam evaporation.

Film thickness measurements were made by the Tolansky multi-beam interferometric technique[21] using glass slides which had been placed in the evaporation system at the same distance from the evaporation source as the specimens. A schematic of the Tolansky technique is shown in Figure 6a. The glass slides were partially masked so that material was only deposited on half of the slide. After deposition the mask was removed and the entire surface covered by evaporating Al, which has high reflectivity. The Al layer follows exactly the contour of the initial film, giving rise to a step on the surface of the slide with a height equal to the thickness of the initial deposited film. When this step is observed in the optical microscope using multi-beam interferometry, a series of stepped fringes are observed (Figure 6b). The distance between successive fringes (L) corresponds to half the wavelength of the incident light (monochromatic radiation from a sodium lamp, 589.3 nm). The ratio of the step height (ΔL) to the fringe width (L) gives a measure of the film thickness.

Hence:

$$t_{film} = \frac{\lambda_{Na}}{2} \frac{\Delta L}{L} \qquad (4)$$

Thicknesses measured using this technique are accurate to within ± 5 nm.

Details of the specimens used in the $\phi(\rho t)$ determination are listed in Table I. When both Cu and Ni evaporations were complete the NaCl substrates were dissolved in water and the films floated onto 3 mm Be grids.

In addition to the interferometry measurements the Ni film thicknesses were also measured using a quartz crystal oscillator[(22)] (Figure 7), and by Talysurf[(23)] measurements. A comparison of thickness measurements made using each technique is given in Table II.

<u>Generation of Data</u>

The $\phi(\rho t)$ curve was determined using the Philips EM400T AEM, in which the electron incidence angle is normal to the sample surface and the x-ray take-off angle $\alpha \simeq 20°$. Intensity measurements from the Cu tracer layer beneath the Ni matrix (I_t) were made at 120 kV and 60 kV using a probe size of 10 nm, and normalized by measuring the intensities from regions not covered by Ni (I_o). A total of 20 measurements were made in both the Cu/Ni and Cu regions to minimize the effect of minor fluctuations in emission current. The maximum count time at each point was 30 seconds and in addition groups of 4 readings were taken alternately from the 2 regions of the specimen. Each intensity reading was corrected for background and measurements made in the Cu/Ni region were corrected for absorption.

Values of $\phi(\rho t)$ for each specimen were obtained by taking the ratio of the Cu intensity from the Cu/Ni region to that of the intensity from the pure Cu region.

Considerations of Specimen Geometry

As mentioned previously, $\phi(\rho t)$ curves can only be determined using the technique outlined if the backscatter coefficient is extremely low. In order to determine the degree of backscatter the thickest specimen (380 nm) was reversed so that the tracer layer was then on top of the foil. X-ray counts were then taken from the isolated tracer layer and also from the tracer layer on top of the Ni matrix. When the latter reading was markedly higher than the former, the backscatter coefficient was considered too high for the determination of the $\phi(\rho t)$ curve. In such cases only the first and last points could be obtained for a particular film thickness. However, for thinner films at the same accelerating voltage, backscatter should not be a problem and so readings were taken from successively thinner, reversed foils until no backscatter was observed. The $\phi(\rho t)$ curve could then be determined for all points up to this foil thickness.

To determine the applicability of this technique for different accelerating voltages, the 380 nm thick specimen was also examined at 80 kV and 100 kV to determine the degree of backscatter.

Statistical Analysis

The determination of $\phi(\rho t)$ curves requires taking the ratio of two values (the Cu x-ray intensity from the Cu/Ni region and that from the pure Cu region) which are very nearly equal to each other. In order to distinguish a true difference between the two values in question, the observed difference in x-ray counts must be greater than the error in the individual readings. This is known as the analytical sensitivity and is expressed mathematically by:

$$\bar{N}-\bar{N}_1 \geq \frac{\sqrt{2}\; t_{n-1}^{1-\alpha}\; S_c}{n^{\frac{1}{2}}} \tag{5}$$

where $\bar{N}$ and $\bar{N}_1$ are the mean x-ray counts from each region, S_c is the standard deviation (which is assumed to be the same for both numbers since they are almost equal), $t_{n-1}^{1-\alpha}$ is the Student t distribution value, and n is the number of counts taken for each set of numbers.

Thus in terms of a percentage, the analytical sensitivity is given by:

$$\text{Sensitivity (\%)} = \frac{\sqrt{2}\; t_{n-1}^{1-\alpha}\; S_c}{n^{\frac{1}{2}}\; \bar{N}} \tag{6}$$

In this work, the Student t value used was that for a 95% confidence limit using 16 measurements.

3. Results and Discussion

The experimental $\phi(\rho t)$ curve for 380 nm of Ni at 120 kV is shown in Figure 8. The error bars represent 95% confidence limits and only the first two data points (for Ni depths of 25 and 55 nm) fail to satisfy the analytical sensitivity criterion (equation 5). This is not surprising since at small depths $\phi(\rho t)$ is very close to unity and the errors in thickness measurement and difficulties in obtaining a uniform film are the greatest.

The $\phi(\rho t)$ data vary by 30% over the thickness range 0 to 380 nm. The curve appears to be approximately linear up to a thickness of 200 nm but above this value $\phi(\rho t)$ increases more significantly with increasing depth.

The error bars imply that up to a thickness of 80 nm the value of $\phi(\rho t)$ does not vary significantly from a value of 1.0 Thus below 80 nm the x-ray production throughout the specimen may be considered uniform. This in turn indicates that the Cu tracer layer used (60 nm) was of suitable thickness that the x-ray production within the tracer could be considered uniform.

The $\phi(\rho t)$ curve for 60 kV is shown in Figure 9. Significant backscatter was observed in all foils $\geq$ 167.5 nm and so the $\phi(\rho t)$ curve could only be determined up to 110 nm. The first few points on the curve (for Ni depths of up to 110 nm) all

failed to satisfy the analytical sensitivity criterion indicating that there was no variation in $\phi(\rho t)$ over this thickness range. For depths > 110 nm only the first and last points of the $\phi(\rho t)$ curve could be determined since $\phi(\rho o)$ was different for each foil thickness. Since the degree of backscatter should vary linearly with foil thickness, the data in Figure 9 has been plotted using a least squares fit to the original $\phi(\rho o)$ data. These results at 60 kV indicate that this technique is unsuitable for $\phi(\rho t)$ determination at low accelerating voltages since the contribution from backscatter is significant.

$\phi(\rho o)$ values for the 300 nm foil were also determined at 80 kV and 100 kV and the results are given in Table III. At 120 kV and 100 kV $\phi(\rho o)$ was effectively equal to 1 since the analytical sensivitity criterion was not obeyed. Backscatter may therefore be considered negligible at these accelerating voltages and so $\phi(\rho t)$ curves can be determined using this technique. Below 100 kV however, $\phi(\rho o)$ values were always greater than 1, implying that considerable backscatter was occurring in the foil at low acclerating voltages.

It may be concluded from this work, therefore, that this method for determining $\phi(\rho t)$ curves is only suitable for accelerating voltages of $\geq$ 100 kV, for 380 nm of Ni. In addition, the significant variation in $\phi(\rho t)$ at 120 kV observed in this investigation has important implications as far as thin film absorption

corrections are concerned. The assumption that $\phi(\rho t)$ is always equal to 1, as is common practice, is not necessarily a valid one. This work indicates that in the case of a Ni foil at 120 kV, $\phi(\rho t)$ is only equal to 1 for foil thicknesses of ≤ 80 nm, which are rarely achieved in conventional analytical microscopy.

The results of this investigation are compared in Figure 10 with the theoretical $\phi(\rho t)$ curves determined by Kyser[20] and Newbury[24] based on Monte Carlo calculations. Newbury's model appears to agree more closely with the experimental data from this work although it only predicts a 10% increase in $\phi(\rho t)$ over the thickness range investigated. The $\phi(\rho t)$ curve produced by Kyser for Cu x-rays at 100 kV shows only a 5% increase in $\phi(\rho t)$ over the same thickness range. It would be expected therefore that a corresponding curve for 120 kV would show an even smaller increase in $\phi(\rho t)$, since higher energy electrons give smaller variations in $\phi(\rho t)$ over the same thickness range. The difference in the $\phi(\rho t)$ curves calculated by Kyser and Newbury may be attributed to detailed differences in the assumptions and theoretical expressions used in the two Monte Carlo approaches. However, the reasons for the discrepancy between calculated and measured $\phi(\rho t)$ curves are not fully understood. It may be that the Monte Carlo calculations do not accurately describe the scattering processes taking place in a thin foil and thus underestimate the variation of $\phi(\rho t)$ with foil thickness.

Alternately, the experimental technique employed may not be accurate enough for this kind of determination.

However, as has already been discussed by Lorimer,[25] with reference to the initial publication by Stenton, et al.[36] of the above results, if significantly high values of $\phi(\rho t)$ (e.g. 1.3 at 380 nm in Ni) are substantiated it has important implications for calculating absorption corrections. Such deviations of $\phi(\rho t)$ from unity would ultimately specify a thickness limit for the validity of equation 3.

III. FOIL THICKNESS MEASUREMENTS

1. Background

Foil thickness measurements are important in several aspects of quantitative analysis in the TEM. In x-ray analysis the foil thickness must be known to determine when correction factors for x-ray absorption should be applied and also their magnitude (Equation 2, Section II). In addition, the foil thickness must be known to determine the analyzed volume. Recent progress in the quantitation of EELS measurements has indicated another area in which a knowledge of foil thickness is required. When using EELS to analyze for a single element, the value obtained has units of atoms/cm^2.[27] Thus, in order to compare absolute values from different regions of the specimen (of variable thickness) a knowledge of the foil thickness is required. In addition, in energy loss analysis the accuracy of the thickness measurement is critical since the final value is extremely sensitive to this measurement, and suitable specimens are typically <50 nm in thickness. Thus a method capable of measuring variations in thickness from 0-50 nm, with high accuracy, is required.

There are various methods for foil thickness determination, not all of which are applicable to particular situations. Use of extinction distances (ξ_g) measurements under two beam conditions requires tedious calculation or is restricted to systems where

ξ_g has been tabulated. Measurement of the projected width of slip traces or any planar defects requires that they be present in the region of interest. The use of latex balls on either side of the foil has been suggested[28] but this requires dipping the specimen in alcohol which may encourage the formation of carbon contamination. The use of Kossel-Möllenstedt fringes in convergent beam patterns is accurate if such fringes can be observed. In past experience that has not been possible in many thin specimens of engineering materials. Usually, therefore, thickness is determined using the contamination spot separation method, since such spots can easily be generated on all specimens even in a Philips EM400T ion-pumped environment, by simply disengaging the cold finger. Although it is acknowledged that there are errors in such measurements (e.g. the work of Love, Cox and Scott[29]) the ease of the technique counters this drawback. Accordingly contamination spot separation measurements were made on a number of thin films of known thickness in order to determine the accuracy of the technique.

2. Experimental Procedures

The films measured comprised two films of Al and a Cu film which were all produced by thermal evaporation from a heated tungsten filament onto NaCl substrates. The film thicknesses were independently determined using the Tolansky technique in combina-

tion with Talysurf and quartz oscillator frequency measurements, as described previously in section II. Contamination spots were produced on each specimen using a 10 nm probe for several minutes with the specimen set at zero tilt. The thin films were mounted on formvar-coated grids to give sufficient support, but contamination spots were only produced in regions where the support film was incomplete so that the values obtained did not include the thickness of the formvar. The specimen was then tilted until the contamination spot was seen to separate into two sections (Figure 11). The tilt angle, magnification and spot separation distance were then recorded and the film thicknesses determined geometrically. At least ten measurements were made on different areas of each specimen.

3. Results and Discussion

Table IV shows the results of the contamination spot measurements together with the corresponding Tolansky measurements (which are accurate to within $\pm$ 5 nm). The errors observed in contamination spot data are considerably greater for the thinner films both in terms of the variation of readings for the same film thickness and in the error over the Tolansky thickness. This is to be expected, since thin films are more likely to show slight thickness variations and also because the spot separation is considerably smaller for thin specimens and thus harder to measure accurately.

A source of the observed error must be attributed to the

measurement of the spot separation distance after tilting, since such distances are relatively small. Also any error incurred in this measurement is greatly magnified when the actual thickness value is computed. The presence of an existing oxide film and/or contamination layer would also contribute to the observed difference as suggested by Love, et al.[29] However, no diffraction evidence for significant surface oxidation was ever observed and it is not considered reasonable that a contamination layer of 100 nm thick exists. More recently Rae, et al.[30] have suggested that the major source of inaccuracy in the contamination spot method is due to the fact that the contamination spots are surrounded by a disc of contamination which is not clearly visible. Thus the error arises from the selection of points on the image from which the measurement is made. All that can be concluded with certainty therefore, is that the contamination spot separation measurement technique significantly overestimates the actual foil thickness and appropriate precautions should be taken when this is the only technique available to determine thickness.

IV. ELECTRON ENERGY LOSS MEASUREMENTS

1. Background

Electron energy loss spectroscopy (EELS) is a technique for obtaining chemical and structural information by measurement of the energy distribution of electrons which have interacted with a specimen but which still remain part of the primary beam. Electrons of a single kinetic energy (in the range of 20 keV to 1 MeV) are passed through a thin specimen and those which undergo inelastic scattering are identified from their resulting energy loss by passing the transmitted beam through an electron spectrometer. For elemental analysis the most important inelastic events are the ionizations of the inner shells of the atom since these cause discontinuities or edges in the energy loss spectrum at energies characteristic of the particular element. This analysis technique was initially proposed by Hillier and Baker[31] in 1944 but has only recently been exploited, primarily as a result of improved electron optics and more efficient electron spectrometers.

Equipment

Microanalysis using EELS can be accomplished using a fairly simple system in which an electron spectrometer is placed below the camera chamber of a transmission or scanning transmission (STEM) microscope (Figure 12.)[32] The transmitted electrons

are analyzed using an electron spectrometer which collects a large fraction of the electrons and disperses them in a focal plane by an amount depending on their loss of energy relative to the kinetic energy of the incident beam.[33] A well defined spectrum from a specific area of the sample can then be obtained by scanning the energy information over a selecting slit. Electron spectrometers generally have a resolution of 1 eV or less but a resolution of 20 eV is usually adequate for detection of the characteristic edges, even in the most densely populated region of the spectrum (0-700 eV). The spectrometer analyzes all electrons scattered within an angular cone β, which is set by the choice of objective or intermediate aperture (Figure 13).[34] The area for analysis is selected by an aperture located just below the viewing screen and the illumination beam angle α, is set by the mode of operation, TEM or STEM. Energy loss spectra may be recorded and processed directly in a multichannel analyzer (MCA), making microanalysis more convenient.

The Energy Loss Spectrum

A typical energy loss spectrum is shown in Figure 14[34] and is plotted in terms of the transmitted signal $I(E)$ as a function of the energy loss E. It contains a sharp peak at $E = 0$ followed by one or more broader peaks generally in the range 10-50 eV, followed by the characteristic edges at higher energy losses. The peak at $E = 0$ is known as the zero loss peak and is the largest

single component in the energy loss spectrum. This peak contains unscattered electrons which have suffered no interactions in passing through the sample, together with electrons which have interacted with the specimen but lost only small amounts of energy. The peak has a finite width due to the energy resolution of the spectrometer, the spread of energy in the incident beam from instabilities in the accelerating potential and a thermal component if a hot source is used.

Considerable structure is observed in the spectrum from 0-50 eV, due mainly to the excitation of valence or conduction electrons, and these are known as "Plasmon" losses. These excitations occur in metals and alloys which have a large number of free electrons and since many valence electrons are involved they are generally termed "collective excitations." The incident electron loses energy E_p ($\sim$ 20 eV) if it excites a plasmon; this energy loss depends on the free electron density and so can be used to identify the material. The plasmon mean free path is typically 50-150 nm at 100 kV so that in thick specimens the electron may excite more than one plasmon and its total energy loss would be a multiple of E_p. In a typical specimen a large fraction of the transmitted electrons will have lost energy by creating plasmons and the signal intensity in this region may be comparable to that of the zero loss peak. This was the first energy loss process to be used for microanalysis[35] but it is

limited to materials showing good plasmon peaks, such as Al alloys. Transition metals, insulators and organic materials, in which the valence electrons are not free to take part in collective excitation show more complex profiles in the low energy loss region. The losses in this case are mainly due to the excitation or ionization of electrons from various bound states and are generally difficult to interpret.

At higher energy losses (> 50 eV) the energy loss spectrum consists of inner shell ionization edges superimposed on a smoothly falling background. The background contains no microanalytical information and arises from a number of effects such as the excitations from valence states to vacuum, multiple plasmon losses, and the tails of edges at lower energy losses. In a multi-element system, each successive edge will contribute to the background intensity of edges at higher energy losses, since unlike x-ray peaks, edges are of indefinite extent. The characteristic edges of interest are superimposed on a rapidly changing background. Each edge represents the energy loss associated with the ionization of an electron from an inner shell of an atom, which is the first step in the production of a characteristic x-ray. A large amount of analytical information can be obtained from the interactions associated with the excitation of inner shell electrons. For example, the energy loss at which the edge starts is the classical ionization energy of an

atom and is uniquely characteristic of that element. These characteristics energy losses have been tabulated[36] as shown in Figure 15. In addition, the shape of the edge is affected by the chemical state, electronic band structure and crystallography of the specimen.[37] Since the inner shell ionization processes are highly localized, they are especially suitable for studies at high spatial resolution.

The mean free path for K x-ray excitation is proportional to the incident electron energy and at 60 kV lies in the range 3-10 μm. This figure is considerably larger than that for plasmon excitation and explains the relatively low intensity of the ionization losses on the spectrum. This is usually compensated for, as shown in Figure 14, by incorporating a gain change in the spectrometer at ∿50 eV to amplify the ionization loss signal.

Shapes of Ionization Edges

The true shape of an ionization edge can only be observed after stripping the background intensity from the spectrum. Although it is not possible to calculate the shape of the background from first principles, it has been found experimentally[38] that the energy differential cross-section of the background has the form:

$$\frac{d\sigma}{dE} = A \cdot E^{-r} \tag{7}$$

where E is the energy loss and A and r are constants depending on the spectrometer acceptance angle, β. Thus for a fixed value of β the background falls as E^{-r} (where r is in the range of 3-5). The background intensity can be subtracted using a method due to Egerton and Whelan,[37] in which the experimental data are plotted on a log-log scale (Figure 16).

K ionization edges arise as a result of the excitation of 1s electrons and are characterized by a sharp rise in intensity followed by a gradual decay of the signal on passing through the edge energy (Figure 17a).[39] The shape of the K edge makes the measurement of its threshold energy relatively easy, and since this is proportional to the atomic binding energy an element can be readily identified from its K edge.

L and M shell ionization edges differ from K edges in that they do not all display a sharp threshold but often have their maximum intensity at an energy loss many eV above the threshold. Such delayed maxima often make identification of L and M edges more difficult. Excitation of the 2p electrons gives rise to L_{23} edges, the shape of which vary considerably with atomic number (Figure 17b). This variation is attributed to the band structure of the elements and is associated with the density of unoccupied states above the Fermi level.[40] M_{45} edges arise from the excitation of 3d electrons and generally do not show sharp discontinuities at the ionization edge, but display a

slow rise in intensity over $\sim$40 eV (Figure 17c).

Edge shapes have also been derived from calculations of ionization cross-sections and have shown reasonable agreement with experiment.[41,42]

Detectability Limits

EELS is not a 'trace sensitive' technique since for a particular element to be detected the number of atoms of that element in an irradiated volume must exceed the minimum detectable number (MDN). When the probe size is small, therefore, the element of interest must be localized, in a precipitate or inclusion. If the element is distributed homogeneously, however, it may be necessary to probe a relatively large volume in order to exceed the detectable limit. The detectability of an element is essentially determined by the visibility of its ionization edge above the background, and may be improved by increasing the incident electron flux or the counting time. For a fixed value of the spectrometer resolution δ, the self-detection limit varies widely with atomic number as shown in Figure 18a.[43] This is attributed to the decrease in ionization cross-section with increasing values of E_K (the energy loss at the onset of an ionization edge). If the spectrometer resolution is allowed to vary such that δ/E_K remains constant, however, the sensitivity can be improved for higher atomic number elements. Thus where possible an optimum spectrometer resolution should be used for each

element, to achieve the best sensitivity. Self detection limits have been determined experimentally for C and Al [41] and values of 10^{-18} g (5×10^4 atoms) and 10^{-17} g (2×10^5 atoms) respectively, were obtained. More often we are concerned with being able to detect a particular element within a matrix of a different element. Joy and Maher [43] have calculated detectability limits for various elements in matrices of C, Si and Fe (representing typical biological, semiconducting and metallic systems). Figure 18b shows the results for the Fe matrix.

In general, experimental values are typically a factor of 10^3 worse than calculated detectability limits due to poor signal to background and signal to noise ratios. Even these practical detectable limits are approximately equal to those attainable by x-ray analysis using STEM.

Quantitation

Much of the current interest in EELS is in its potential for giving rapid quantitative analysis at high spatial resolution, especially for elements in the first two rows of the periodic table ($Z \leq 12$). It has been shown by several authors [38,45,46] that the electrons which have suffered an energy loss even have a small angular distribution around the forward direction and so can be readily collected and analyzed. In addition, unlike x-ray or Auger techniques which require correction or standardization

procedure to give numerical data, the quantitation of EELS, in principle, is both simple and absolute.

A quantitative estimate for the number of atoms per unit area of the specimen (N) is obtained from the area I_K under an excitation edge, after extrapolating and subtracting the background which precedes the edge:[27]

$$N = \frac{1}{\sigma_K} \left(\frac{I_K}{I}\right) \qquad (8)$$

In this equation, I is the incident electron current and is equal to the area under the entire spectrum and σ_K is the total cross-section per atom for excitation of the K shell for a particular energy of the incident beam. Similar equations can be used for L and M edges provided the appropriate values of σ_L and σ_M are known.

Most spectrometers, however, do not have sufficient acceptance angle to measure I_K while maintaining good energy resolution. This problem is overcome by placing an aperture (generally the objective aperture, in TEM mode) after the specimen to limit electron scattering to angles less than β (sometimes referred to as α by other authors).[27] A core loss signal $I_K(\beta)$ can then be measured with increased signal:background and signal:noise ratios. However, in most microanalysis situations the excitation edge is superimposed on a large background and so the resulting statistical accuracy in $I_K(\beta)$ is poor. The background extrapolation may also

be seriously in error if excitation edges of other elements occur within the range of extrapolation. These errors are reduced by measuring the edge intensity over an energy range Δ above E_K. Equation (8) then becomes:

$$N = \frac{1}{\sigma(\beta,\Delta)} \frac{I_K(\beta,\Delta)}{I_o(\beta,\Delta)} \qquad (9)$$

where $\sigma(\beta,\Delta)$ is the partial ionization cross-section corresponding to inner-shell losses between E_K and $E_K + \Delta$, $I_K(\beta,\Delta)$ is the intensity of the edge measured through the aperture β for an energy window Δ, and $I_o(\beta,\Delta)$ is the intensity measured from 0 eV loss to ΔeV (i.e. an energy window of Δ around the zero loss peak).(Figure 19).[47]

Ratio Method

If only the relative amount of two elements are required (i.e., N_1/N_2) then a ratio technique can be used, as in x-ray microanalysis. Provided that the two excitation edges are measured under the same experimental conditions (from the same spectrum and using the same energy window Δ), the intensity $I_o(\beta,\Delta)$ will be the same for both edges and therefore cancels. The ratio is then given by:

$$\frac{N_1}{N_2} = \frac{\sigma_{K_2}(\beta,\Delta)}{\sigma_{K_1}(\beta,\Delta)} \cdot \frac{I_{K_1}(\beta,\Delta)}{I_{K_2}(\beta,\Delta)} \qquad (10)$$

Thus the ratio can be determined by measuring the inner shell

losses $I_{K_1}(\beta,\Delta)$ and $I_K(\beta,\Delta)$ provided that $\sigma_{K_1}(\beta,\Delta)$ and $\sigma_{K_2}(\beta,\Delta)$ are known or can be calculated.

Operating Conditions

Although the equations in the preceding section are not exact, they can be made sufficiently accurate by the correct choice of operating conditions and careful sample preparation.

(a) Spectrometer acceptance angle (β): The background energy losses have a broader angular distribution than the inner shell excitation signals and so the signal to background ratio can be improved by decreasing the size of the acceptance angle of the spectrometer (β). Egerton et al.[48] indicated that there is an optimum collection aperture for each characteristic energy loss. In general, however, β should be ~ 10 mrad for K shell excitations of the first row elements.[47]

(b) Energy window (Δ): The choice of a suitable range of Δ for the integration of the characteristic signal is determined by two opposing considerations. As Δ is decreased below 50 eV the accuracy of equations (9) and (10) is decreased and the signal and the signal:noise ratio are worse for small energy windows. As Δ is increased, however, the accuracy of the background subtraction becomes poorer since there is a greater probability of excitation edges of other elements appearing within the range of integration. For most situations an energy window between 50 and 150 eV is recommended.[50]

(c) Specimen orientation: For single crystal or polycrystalline specimens the accuracy of equations (9) and (10) depends on the location of any strong diffraction spots relative to the objective aperture. The maximum error occurs when a strong diffraction spot, falls just outside or just inside the aperture.[51] Strong Bragg reflections should also be avoided since they remove electrons from the main beam and so reduce the characteristic loss signal.

(d) Specimen thickness: Thick specimens may cause large discrepancies in quantitation because it is likely that the incident electrons will interact more than once with the sample before they leave. Such plural scattering reduces the signal: noise ratio and so makes identification of edges difficult and in some cases may alter the shape of the edge significantly. It is, therefore, recommended that the specimen thickness should be less than the mean free path for plasmon excitation (λ_p), or more generally, the mean free path for the inelastic scattering events.[52] For most materials this implies that the specimen thickness should be less than 100 nm. More recent work,[53] however, has suggested that the optimum thickness for quantitative analysis is $\sim 0.2\ \lambda_p$ which is considerably less than the thickness of conventional TEM samples.

Determination of Partial Ionization Cross-Sections

Quantitative analysis is only possible if values for the

partial cross-section $\sigma(\beta, \Delta)$ are known or can be calculated. Total ionization cross-sections have been calculated by a variety of methods and have been measured experimentally from x-ray and Auger analysis. Partial cross-sections, however, have not been tabulated at all, owing to the large number of values which would be necessary to cover all parameters relevant to EELS. There are three main methods by which $\sigma(\beta, \Delta)$ can be determined, as outlined by Joy, et al.[27] The most commonly used method is to calculate values of $\sigma(\beta, \Delta)$ from a simple model which relates the partial cross-section for any elemental species to that of the hydrogen atom. For conditions normally used in TEM energy loss analysis, this hydrogenic approximation gives results which are in good agreement with experimental data for K shell losses. Values for $\sigma(\beta, \Delta)$ can be rapidly calculated using a short Fortran program (SIGMAK).[54] The only inputs required are the threshold energy E_K, the energy window Δ, the accelerating voltage E_o, the scattering angle β, and the atomic number Z. A similar program SIGMAL[55] can be used for L shells based on the same approximation with some minor corrections. A more sophisticated technique has recently been suggested[42] which gives more accurate values of $\sigma(\beta, \Delta)$ for L losses and is also applicable to M shell losses.

Partial cross-sections may also be determined by the "efficiency factors" method[27] in which the variables β and Δ can be

treated separately in terms of their effect on $\sigma(\beta,\Delta)$ such that:

$$\sigma(\beta,\Delta) = \sigma_T \, n_\beta \, n_\Delta \tag{11}$$

where σ_T is the total ionization cross-section and n_β and n_Δ are the efficiency factors relating to the spectrometer acceptance angle and the energy window respectively. Values for n_β and n_Δ can be determined analytically from the shape of the edge. Alternately, $\sigma(\beta,\Delta)$ can be determined by using a separate experiment on a standard specimen.[(27)]

Quality of Experimental Results

There are three main criteria for establishing the quality of a particular quantitation technique:

(a) The measurement of N should remain constant when the experimental parameters are varied.

(b) Measurements of the composition of compounds of known stoichiometry should agree with the expected results.

(c) The value of N should agree with measurements made by independent quantitation methods and also with similar measurements made on different instruments.

If only the first two criteria are satisfied, the technique may be used for relative quantitation, but standards would be required to obtain absolute values. If all three criteria are obeyed, however, the technique may be considered an absolute

quantitative method.

Joy, et al.[27] tested the applicability of each of these three criteria to the quantitation of 'standard' specimens, using EELS. The accelerating voltage and spectrometer acceptance angle are generally fixed by the mode of microscope operation in EELS and so the stability of N with respect to different experimental parameters was tested by varying Δ. It was found that N remained stable to within 5% for Δ between 30 to 300 eV for K shell ionization using the SIGMAK program. Similarly, the SIGMAL program for L shell ionizations gave values of N which were stable to $\leq$15% between 50 to 500 eV. It was, therefore, concluded that the calculated cross-sections method satisfied the first criterion for both K and L edges.

The accuracy of elemental ratios was determined using two standard compounds containing light elements, namely BN and MgO. The calculated cross-sections method gave values of N for Mg and O which remained stable with Δ and gave a resultant atomic ratio (Mg:O) of 0.93 ± 0.03, which is in good agreement with the expected value. Thus elemental ratios involving K losses were obtained with an accuracy of 10% or better.

In theory, absolute quantitation by EELS should be fairly simple since no corrections for absorption or fluorescent yield are required. This aspect was examined by comparing results with those obtained from the same specimen area by independent tech-

niques. The general level of agreement between the EELS data obtained using the calculated cross-sections technique, and independent measurements was good, although a systematic discrepancy of ∿25% was observed between values obtained at 80 and 100 kV. It was not possible to assess which acclerating voltage gave the more accurate result, since the density of the carbon film could not be determined sufficiently accurately. The error may be attributed to the instrumental artefacts or the limited knowledge of ionization cross-sections at high voltages but is more likely to be due to specimen defects such as thickness variations, carbon contamination, or loss of mass.

In summary, therefore, Joy, et al.[27] have shown that under suitable conditions a stability of $\pm$ 5% with respect to variations in experimental parameters is attainable, a relative accuracy of 10% or better can be expected when analyzing compounds and an absolute accuracy of $\pm$ 20% should be possible.

Comparison of Energy Loss and X-ray Analysis

The major differences between energy loss and x-ray analysis may be summarized as follows:

(a) Energy loss measurements are concerned with the primary excitation of electrons whereas x-ray production is a result of the secondary decay of these excitations.

(b) For light elements energy loss analysis becomes more efficient as the atomic number decreases due to an increase in

the ionization cross-sections for light elements. X-ray detection from light elements is very poor, however, because only a small percentage of the K shell ionizations produce x-rays (the rest produce Auger electrons) and many of the x-rays produced are absorbed by the window and Si dead layer of the detector.

(c) Energy loss analysis is less efficient for high atomic number elements due to the decrease in the ionization cross-sections and the poor signal to noise ratio at higher energy losses. X-ray analysis is, therefore, recommended for high atomic number elements.

(d) Electrons which have undergone ionization are scattered through very small angles only and so most of the signal can be detected and recorded. X-rays, however, are emitted uniformly in all directions and the detector generally only subtends a small angle at the specimen and so the collection efficiency is very poor.

(e) Since almost all of the ionization events are measured in EELS it is possible to detect the presence of very low concentrations ($\sim 10^{-18}$ g).

(f) Although energy loss quantitation has the potential for giving absolute concentrations, analysis of multi-component systems is not very accurate due to the contribution of edges at low energy losses to the background intensity of subsequent

edges. This is not a problem in x-ray analysis, however, since x-ray peaks have a relatively small, finite width.

(g) Specimens for EELS must be extremely thin (generally <50 nm) to prevent plural scattering events which lower the signal to background ratio. Thus more careful preparation of samples is required than for x-ray analysis.

(h) In EDS analysis, using STEM, the x-ray spatial resolution is ~ 50 nm, whereas in EELS a spatial resolution of 10 nm is attainable.

2. Experimental Procedures

Specimen Preparation

The material used in this investigation was a directionally-solidified eutectic in the calcia-zirconia system which had been grown in a commercial crystal growing furnace,[56] at a rate of 0.8 cm/hr. The initial composition of the melt was ~ 77 wt% ZrO_2 which gave rise to a eutectic consisting of $CaZrO_3$ and ZrO_2 solid solution containing CaO (subsequently referred to as $ZrO_{2(ss)}$) in accordance with the recent phase diagram due to Stubican and Hellman[57] (Figure 20).

Thin foils were prepared by sectioning the directionally solidified eutectic perpendicular to the direction of growth and grinding the sections down to <50 μm using SiC powder (320 through 1000 mesh). The sections were then ion-beam thinned in argon at 6 kV at an angle of 13° and coated with a thin layer

of evaporated carbon or aluminum to prevent charging in the microscope.

EDS Analysis

$CaZrO_3$ is a stoichiometric compound phase of fixed composition whereas $ZrO_{2(ss)}$ is a nonstoichiometric solid solution phase with a defect fluorite structure. Substitution of Ca^{2+} for Zr^{4+} in the solid solution gives rise to anion (O^{2-}) vacancies, in order to maintain charge neutrality. The general formula for $ZrO_{2(ss)}$ is therefore given by:

$$Ca_x\ Zr_{1-x}\ O_{2-x} \qquad (12)$$

Prior to EELS analysis it was necessary to use EDS to determine the exact compostion of the $ZrO_{2(ss)}$ phase and also to determine whether or not local cation segregation was occuring particularly at the lamellar interfaces. Thus x-ray analyses were performed on a Philips EM400T microscope with an EDAX 9100 energy dispersive detector.

(a) Determination of K_{Ca-Zr}

Calculations indicated the x-ray absorption was negligible in both phases of this system (Appendix I) and so the standardless ratio technique using the Cliff-Lorimer[(2)] equation could be applied. This method involves measuring the x-ray intensity ratio I_A/I_B of two elements A and B in a thin foil simultaneously. This intensity ratio can be related directly

to the ratio of the mass concentrations $^{C_A}/_{C_B}$ such that:

$$\frac{C_A}{C_B} = k_{AB} \frac{I_A}{I_B} \qquad \text{(Equation (1), Section I)}$$

The constant k_{AB}, knownas the "k factor" varies with the operating voltage and to a certain extent with the instrument used (due to variations in detector geometry and contamination characteristics) but it is independent of the composition. Although k factors can be calculated theroetically from considerations of the x-ray production in the thin foils, recent work[58] has suggested that these values are somewhat in error, especially when using L or M shells. It is advisable therefore that the k factor be determined accurately for the individual system of interest and that identical conditions be used for analysis.

The k factor for Ca-Zr was determined using the $CaZrO_3$ phase, since the exact composition could be determined assuming fixed stoichiometry. A total of 25 spectra were collected at random points throughout the $CaZrO_3$ phase using a probe size of 10 nm and obtaining a minimum of 10,000 counts in each peak. However, regions close to the $CaZrO_3/ZrO_{2(ss)}$ interface were avoided to eliminate regions of possible cation segregation. Integrated intensities under the Zr-L and Ca-K peaks were obtained using the Tracor Northern MTF program. All intensities were normalized with respect to Zr and the concentration ratio of the elements was used to obtain a value of k_{Ca-Zr}. The relative error in the

k factor value was determined using an equation due to Goldstein[59]

$$\% \text{ error} = \left[\frac{t_{95}^{n-1}\ \sigma}{\sqrt{n}\ \ k_{avg.}}\right] \times 100 \qquad (13)$$

where t_{95}^{n-1} is the student t value for n readings at a 95% confidence limit, σ is the standard deviation for n readings and $k_{avg.}$ is the average k_{Ca-Zr} value. For 25 values $t_{95}^{24} = 2.064$ (from statistical tables), and so the value of k_{Ca-Zr} using a 95% confidence interval was determined to be:

$$k_{Ca-Zr} = 0.692 \pm 0.007$$

(b) Determination of the Composition of $ZrO_{2(ss)}$

Having determined a value for k_{Ca-Zr}, the exact composition of the cations in $ZrO_{2(ss)}$ could then be found using the Cliff-Lorimer relationship (equation 1). A total of 25 spectra were collected from random points in the $ZrO_{2(ss)}$ phase (avoiding lamellar interfaces) using a probe size of 10 nm and a count time of 100s. The composition was determined using the Tracor Northern MTF program after inputting the previously determined value of k_{Ca-Zr}. The relative error in composition was determined using equation (13) and, in terms of the cation concentration, the composition was:

10.04 $\pm$ 0.06 wt% Ca

89.96 $\pm$ 0.06 wt% Zr

Since conventional EDS is not capable of detecting elements with atomic number <11 the oxygen content in $ZrO_{2(ss)}$ was determined from equation (12) based on considerations of charge neutrality. In terms of mol% the composition of the $ZrO_{2(ss)}$ phase was determined to be:

20.23 ± 0.12 mol% CaO

79.77 ± 0.12 mol% ZrO_2

(c) Profile Across a Lamellar Interface

EDS profiles were performed across $CaZrO_3/ZrO_{2(ss)}$ lamellar interfaces to determine if any cation segregation was occurring in these regions. In each case, care was taken to orient the interface parallel to the electron beam and analyses were made along a line perpendicular to the interface at 120 kV, using a probe size of 10 nm. Calculations of beam broadening in the two phases are given in Appendix II. For a typical thin foil ($\sim$200 nm thick) the beam broadening was found to be 32.2 nm in $CaZrO_3$ and 37.1 nm in $ZrO_{2(ss)}$, assuming the electron beam to be a point source. However, since a probe size of 10 nm was used, this value should be added to the calculated values of beam broadening to give a better estimate of the total beam broadening. To ensure there was no overlap between the regions analyzed therefore, the probe was moved in 50 nm steps across the interface. The data were converted into weight

percentage using the Tracor Northern MTF program using a value of 0.692 for k_{Ca-Zr}.

X-ray counting statistics obey Gaussian behavior and so the relative error in each analysis is given by $\sigma = \sqrt{N}$, where N is the number of accumulated counts. Thus the relative standard deviation in a single measurement of N counts is:

$$\sigma_{rel} = \frac{\sqrt{N}}{N} \qquad (14)$$

At a 95% confidence level the percentage relative error is given by:

$$\%\ Error_{rel} = \frac{3\sqrt{N}}{N} \times 100 \qquad (15)$$

Since the Cliff-Lorimer equation utilizes the x-ray intensity ratio I_{Ca}/I_{Zr} the relative error involved is the sum of the errors in I_{Ca} and I_{Zr}. Values for the relative errors in I_{Ca} and I_{Zr} were calculated for a 95% confidence level using equation (15).

In addition, there is also an error associated with the experimentally determined k factor, k_{Ca-Zr}, and this was also added to the relative error in I_{Ca} and I_{Zr}.

The horizontal errors representing the spatial resolution of the x-ray information were calculated from the sum of the probe diameter and the calculated beam broadening in the specimen.

Although beam broadening is a function of specimen thickness, it was assumed that the specimen was 200 nm thick at all analysis points in the profile, since the only suitable method for measuring specimen thickness in the present case (the contamination spot method) has been shown to be susceptible to inaccuracy (section III).

EELS Analysis

(a) Energy Loss Analysis on the Philips EM400T

Energy loss analyses were performed on the Philips EM400T fitted with a Gatan 607 energy loss spectrometer. Details of the spectrometer design and operation mode are given in the Gatan Instruction Manual.[60] All analyses were performed in the TEM imaging mode in which a normal image is formed on the viewing screen while the projector cross-over contains a small diffraction pattern. This mode of operation permits the selection of a small specimen area for microanalysis while a large area is being illuminated. Hence the TEM imaging mode is particularly useful for specimens which are beam-sensitive or prone to carbon contamination.

After setting up the spectrometer (described in detail in the Gatan Instruction Manual) the region to be analyzed is selected by the spectrometer entrance aperture located below the viewing screen. This corresponds to a region 5 mm in diameter at the center of the viewing screen. The actual area of material

analyzed is then governed by the magnification setting (i.e. at a higher magnification a smaller area is analyzed). The spectrometer acceptance angle, β, is governed by the size of the objective aperture. Details of converting the aperture diameter into the semi-angle β, are given in Appendix III and listed in Table V. Having set the specimen at 0° tilt (to minimize the thickness of specimen through which the electrons must travel) and positioning the area of interest at the center of the viewing screen the beam is condensed on the region of interest and the viewing screen lifted. Spectra can then be acquired using the Tracor Northern 2132 ELS program.

It is generally recommended that several sweeps across the energy spectrum be performed in order to improve the signal to noise ratio of the spectrum. However, it was found that the energy calibration drifted significantly between sweeps and so the edge information became distorted. Thus only one sweep was performed at each analysis point and the dwell time on each channel was increased to 1 or 2 seconds, to improve the signal to noise ratio.

The energy loss data were quantified using the Tracor Northern TN-2132, Version 2, ELS program. At the present time this program only permits complete quantitation of K edges via the SIGMAK program. However, the program can also be used to determine the integrated counts under other types of edges. Therefore, by

obtaining values of $\sigma_L(\beta,\Delta)$ from an independent SIGMAL program (due to Joy[61]), L edges can also be analyzed using equation 9.

(b) <u>Determination of $^{Ca}/_{O}$ Atomic Ratios</u>

The $^{Ca}/_{O}$ ratios in each of the phases in the $CaZrO_3$/$ZrO_{2(ss)}$ eutectic system can be calculated independently of the EELS measurements. In the case of $CaZrO_3$ the $^{Ca}/_{O}$ ratio can be calculated directly from the stoichiometry and in the case of $ZrO_{2(ss)}$ it may be determined from EDS measurements in combination with considerations of charge neutrality. Thus by comparing the experimental ratios obtained from EELS with the calculated $^{Ca}/_{O}$ ratios the accuracy of the present EELS quantitation technique may be assessed.

A minimum of 25 EELS spectra were collected from each phase of the eutectic for each operating condition. Regions close to the lamellar interfaces were avoided and spectra were generally collected from areas adjacent to the ion-thinned hole, since these were the thinnest regions of the specimen. All spectra were collected at an operating voltage of 120 kV and a magnification of 20,000 which corresponds to an analysis area 250 nm in diameter. The spectrometer acceptance angle β, was varied by using different objective aperture sizes and the spectra were analyzed using different values of Δ (the energy range of integration) for both the background fit and edge intensity.

Since it was necessary to coat the specimens to prevent them

from charging in the microscope, EELS analyses were performed on both carbon and aluminum coated specimens. Since both these elements have edges which lie in the same energy range as the major edges from the elements in the sample (Figure 15), they may affect the accuracy of the quantitation.

A complete list of the operating and analysis parameters used for each set of analyses is given in Table VI. The $^{Ca}/_{O}$ ratios (N_{Ca}/N_{Ox}) were determined by substituting the appropriate parameters into equation (10) to give the following expression:

$$\frac{N_{Ca}}{N_{Ox}} = \frac{\sigma_{K_{Ox}}(\beta,\Delta)}{\sigma_{L_{Ca}}(\beta,\Delta)} \cdot \frac{I_{K_{Ox}}(\beta,\Delta)}{I_{L_{Ca}}(\beta,\Delta)} \qquad (16)$$

where $\sigma_{K_{Ox}}(\beta,\Delta)$ and $\sigma_{L_{Ca}}(\beta,\Delta)$ are the partial ionization cross-sections for the oxygen K shell and calcium L shell, respectively and $I_{K_{Ox}}(\beta,\Delta)$ and $I_{L_{Ca}}(\beta,\Delta)$ are the integrated intensities under the corresponding edges.

The integrated intensities were obtained using the Tracor Northern ELS program and the partial cross-sections were obtained from the SIGMAK and SIGMAL programs due to Joy.[61] Complete listings of the partial cross-sections for the oxygen K shell and calcium L shell, for various values of β and Δ, are given in Tables VII and VIII respectively.

(c) EELS Profiles

In addition to obtaining average $^{Ca}/_{O}$ ratios from each

phase, as described in the previous section, $^{Ca}/_{O}$ ratios were also determined from EELS profiles across lamellar interfaces. Such profiles would test the sensitivity of the quantitation method to a relatively large change in the $^{Ca}/_{O}$ ratio at the interface.

Profiles were taken in regions of the specimen where a $CaZrO_3/ZrO_{2(ss)}$ interface intersected the ion-thinned hole, by acquiring spectra along the edge of the hole passing from one phase to the other. Spectra were collected under a variety of operating conditions, listed in Table IX, at a magnification of 20,000 and moving in steps of 500 nm across the interface. $^{Ca}/_{O}$ ratios were determined from the integrated intensities under the appropriate edges, as described in the previous section.

The vertical error bars were determined from the counting statistics based on a 95% confidence level, using equation (15). In addition, a further estimated error of 10% was added, to account for the errors in the calculated partial cross-sections. The horizontal error bars represent the diameter of the area analyzed plus an additional 20% of this value to account for estimated errors in the step size. At this time, there appears to be no more definitive means of calculating these estimated errors, but rather they are felt to be reasonable values based on operator experience.

3. Results and Discussion

Microstructure of the Eutectic

A low magnification photomicrograph of a section of the directionally solidified eutectic cut perpendicular to the direction of growth is shown in Figure 21. This micrograph was taken from a petrographically thinned section using optical transmission microscopy. The lamellae have a very uniform spacing (~ 7 μm); the light phase being $CaZrO_3$ and the dark phase $ZrO_{2(ss)}$. Figure 22 shows the same structure observed in TEM. The $ZrO_{2(ss)}$ phase shows darker contrast because it has a higher Zr content and higher atomic number elements, such as Zr, absorb electrons more readily.

(i) $ZrO_{2(ss)}$ Phase

Figure 23 shows a [100] diffraction pattern from the $ZrO_{2(ss)}$ phase, confirming the cubic nature of the solid solution. However, this pattern was not typical of those generally obtained from the $ZrO_{2(ss)}$ phase; more often the diffraction patterns contained diffuse "donut" shaped features as shown in Figures 24a and 24b. The appearance of these diffuse diffraction features appeared to be associated with the observation of a mottled contrast effect in the bright field image, Figure 25. However, attempts to produce centered dark field (CDF) images corresponding to the diffuse features on the diffraction pattern failed to reveal any useful information. Both the diffuse diffraction features and

the mottled contrast have been observed by other workers in both partially and fully stabilized $CaO-ZrO_2$ systems.[62-67] Similar effects have also been observed in zirconia systems containing other stabilizing cations.[63, 68]

Carter and Roth[62] together with Schoenlein, et al.[63] have attributed this effect to the cooperative ordering of oxygen ions on the oxygen sublattice at low temperatures. Allpress and Rossell,[64] however, proposed that the effect was due to domains of the ordered compound $CaZr_4O_9$, embedded coherently in the cubic matrix. Hudson and Moseley[65] showed that the diffuse scattering was of greatest intensity at 20 mol% CaO, adding further evidence to the $CaZr_4O_9$ domain theory. However, Cohen, et al.[66] calculated the intensities for diffuse scattering, assuming the presence of $CaZr_4O_9$ domains of appropriate size, and found that these did not agree with the observed intensities. Furthermore, Rossell[67] has observed the diffuse intensity in specimens quenched from high temperatures (also observed in this investigation). The formation of microdomains of $CaZr_4O_9$ during quenching is unrealistic because the order/disorder temperature is 1000°C (Figure 20) and the Ca ions could only move 0.05 nm s^{-1} at this temperature. When such quenched specimens showing diffuse diffraction features are annealed for long periods at 1400°C, however, the diffuse features become groups of spots corresponding to crystallites of $CaZr_4O_9$. It

would appear, therefore, that the diffuse features are in some way associated with the formation of $CaZr_4O_9$ and may be due to local ion displacements in the structure which contribute to the formation of $CaZr_4O_9$ on annealing.

(ii) $CaZrO_3$ Phase

The major feature of the $CaZrO_3$ phase was the presence of numerous boundaries such as those seen in Figure 26. In some cases these were believed to be low angle boundaries, since such features as bend contours remained almost continuous across the interface, Figure 27. In most cases, however, a very distinct fringe contrast was observed at the boundary. These fringes were asymmetrical in bright field, Figure 28a, and symmetrical in dark field, Figure 28b, showing the major characteristics of δ boundaries.[69] δ boundaries are defects separating two regions of a crystal with different values of $\underline{s}$ or $\underline{g}$ for the same operative reflection. These boundaries have been reported in several oxide systems[70-72] and generally arise from an ordering process which gives rise to differently distorted regions within a crystal. Similar features have been observed in $BaTiO_3$[72] which is isostructural with $CaZrO_3$. In the case of $BaTiO_3$, the boundaries arise from lattice deformations accompanying the spontaneous polarization of this ferroelectric material; $CaZrO_3$ however is not ferroelectric. The cause of the δ boundaries in $CaZrO_3$ is unknown, although selected area diffraction patterns (SADPs)

taken from various regions of this phase have revealed at least three variations in the crystallography. In some areas the high temperature ordered, cubic form of $CaZrO_3$ had been retained, Figure 29. In other regions, however, cubic diffraction patterns with a larger lattice parameter have been recorded, Figure 30. In other regions diffraction patterns have been recorded which appear to be non-cubic, Figure 31. This suggests that the δ boundaries may be associated with regions of different crystallography, however, further investigation of this phenomena is required before the exact nature of the boundaries in $CaZrO_3$ can be determined.

EDS Analysis

Despite the anomalies in the microstructure of the two phases (i.e. the mottled contrast in $ZrO_{2(ss)}$ and the boundaries in $CaZrO_3$) EDS analysis indicated that both phases were chemically very homogeneous. Typical spectra from each phase are shown in Figure 32. The compositions (in terms of wt% of cations), determined from a total of 25 readings from random points in each phase gave the following results.

$CaZrO_3$	30.53 ± 0.31 wt% Ca
$ZrO_{2(ss)}$	10.04 ± 0.06 wt% Ca

The relative errors (determined for a 95% confidence level using a student t value for 25 readings) are very small, indica-

ting a high degree of homogeneity.

The results of an EDS profile taken across a lamellar interface are shown in Figure 33. As discussed previously, the vertical error bars represent the sum of the errors in the counting statistics for each element and the error in the experimentally determined k factor. The horizontal error bars represent the spatial resolution of the x-ray information; that is, the sum of the probe diameter and the beam broadening. This profile indicates that there is no appreciable segregation of cations in the region of the $CaZrO_3/ZrO_{2(ss)}$ interface. This implies that there would be no segregation of oxygen ions at the interface either, since this would give rise to regions of local charge imbalance which would have to be reflected in a change in cation concentration since both cation species have only one stable valence.

EELS Analysis

(i) Visual Comparison of Spectra

Figures 34a and 34b show typical EELS spectra from the $CaZrO_3$ and $ZrO_{2(ss)}$ phases, respectively. The two spectra show distinct differences for example, the $Ca_{L_{23}}$ edge is much larger in the $CaZrO_3$ phase, and the $Zr_{M_{45}}$ and $Zr_{M_{23}}$ edges are somewhat smaller, as would be expected from the compositions. The large carbon edge is due to the carbon coating on the foil.

Figures 35a and 35b show the effect of the objective aperture size on the spectra. Figure 35a is a spectrum taken

from the $CaZrO_3$ phase using the 100 μm objective aperture (corresponding to a spectrometer acceptance angle β of 9.73 mrads). Figure 35b is a spectrum taken from the same area using the 50 μm objective aperture (β = 4.86 mrads). Comparing these two spectra it can be seen that the use of a smaller objective aperture increases the height of an edge relative to the background signal. In addition, the shape of the Zr edge is more easily distinguished using the 50 μm aperture. These effects are even more pronounced in the corresponding spectra taken from the $ZrO_{2(ss)}$ phase. Figure 36a shows the spectrum obtained in this phase using the 100 μm objective aperture and Figure 36b is the spectrum from the same area using the 50 μm objective aperture.

The reason for the improved peak to background ratio at a smaller aperture size is associated with the angular distribution of the core-loss and background signals. The core-loss signal (due to the inner shell excitations) has a relatively narrow angular distribution (a few mrads) whereas the angular distribution of the background losses is somewhat broader. Thus when a smaller objective aperture size is used the core-loss signal remains essentially unchanged but the background signal is limited by the aperture and this results in an improved signal to background ratio.

Typical spectra from the Al coated specimens are shown in Figure 37. Figure 37a is the spectrum from the $CaZrO_3$ phase and Figure 37b is from the $ZrO_{2(ss)}$ phase. The major Al edge occurs at the low energy loss end of the spectrum, at ~70 eV (not visible in Figure 37) and it would appear that the tail of this edge has almost completely masked the information from the $Zr_{M_{23}}$ and $Zr_{M_{45}}$ edges. The $Ca_{L_{23}}$ and O_K edges are still clearly visible however.

(ii) Evaluation of $^{Ca}/_{O}$ Ratios

From considerations of stochiometry the $^{Ca}/_{O}$ ratio in $CaZrO_3$ is 1/3 (0.3333). EDS analysis of the $ZrO_{2(ss)}$ phase indicated that it contained 10.04 ± 0.06 wt% Ca (in terms of the cations only) corresponding to ~20 atomic% Ca. From considerations of charge neutrality and the oxide stoichiometry in the system, this gives the following fomula for the $ZrO_{2(ss)}$ phase:

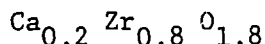

$$Ca_{0.2}\ Zr_{0.8}\ O_{1.8}$$

Hence the $^{Ca}/_{O}$ ratio for $ZrO_{2(ss)}$ is 1/9 (i.e. 0.1111). The experimentally determined $^{Ca}/_{O}$ ratios from EELS analysis, for different operating and analysis conditions are given in Table X. Inspection of these experimental results indicate that the $^{Ca}/_{O}$ ratios for $CaZrO_3$ are consistantly higher than the corresponding $ZrO_{2(ss)}$ ratios, as predicted, and both sets of

numbers show the correct order of magnitude. The errors were calculated for a 95% confidence level using a student t value for 25 readings.

(a) Effect of Objective Aperture Size

The spectrometer acceptance angle β is governed by the objective aperture size, as discussed previously. Table XI shows the effect of the objective aperture size on the $^{Ca}/_{O}$ ratios, when all other experimental parameters were maintained constant. Despite the improved signal to background ratio observed using the 50 μm aperture (β = 4.86 mrads), the aperture size appeared to have little effect on the resultant $^{Ca}/_{O}$ ratio. From Table XI it can be seen that the $^{Ca}/_{O}$ ratio remained unchanged for the $CaZrO_3$ phase whichever aperture was used. Slight variations in the ratio were observed in the $ZrO_{2(ss)}$ phase but these were attributed to scatter in the experimental data rather than a systematic variation due to the aperture size.

(b) Effect of Energy Window

Different energy windows for both the background and edge fits were selected for the analyses. Under ideal conditions the $^{Ca}/_{O}$ ratio should not vary with Δ, since for any change in Δ there is a corresponding change in $\sigma(\beta, \Delta)$. This was found to be so in the case of the carbon coated specimens, where the $^{Ca}/_{O}$ ratio appeared to be unaffected by a change in Δ. For the Al coated specimens, however, the choice of energy window had a

marked effect on the $^{Ca}/_{O}$ ratio. In particular the $^{Ca}/_{O}$ ratios from the $ZrO_{2(ss)}$ phase showed considerable discrepancies when a 50 eV edge window was used rather than a 20 eV window. In the former case, the ratio was a factor of 10 lower than the predicted value and there was also considerable spread in the data, indicated by a relative error of 38%.

The reason for these discrepancies is attributed to the background fit to the $Ca_{L_{23}}$ edge. The TN-2132 ELS program used to analyze the spectra is not able to strip out edges prior to the edge of interest. Therefore, when setting up energy windows for the background extrapolation, the background was chosen as the region immediately prior to the onset of the edge. For the oxygen edge at 531 eV this did not present any problems because the background intensity falls fairly smoothly over a wide energy range prior to the onset of the O_K edge (Figure 38). However, the background fit to the $Ca_{L_{23}}$ edge (at ∿350 eV) was complicated by the presence of the $Zr_{M_{23}}$ edge at ∿340 eV. Since there was no means of stripping the $Zr_{M_{23}}$ edge out of the spectrum the background fit was considerably distorted by the presence of edge, as seen in Figure 39. This gave erroneous numbers for the integrated intensity under the Ca edge and corresponding errors in the final $^{Ca}/_{O}$ ratio.

It might be expected that the problem of the background fit to the Ca edge would be even greater for the carbon coated specimens, due to the presence of a large C_K edge at 285 eV (Fig-

ure 35). However, it was found that fitting the Ca background window to the C edge gave a reasonable background extrapolation to the Ca edge, Figure 40 (since the major contribution to the Ca background intensity is the tail of the C edge). In addition, the presence of the C_K edge tended to mask the effect of the $Zr_{M_{23}}$ edge, and so there was little distortion to the background fit.

(c) Deviation from Predicted Values

Although the experimentally determined $^{Ca}/_{O}$ ratios remained relatively stable to changes in β and Δ as discussed above, they showed considerable deviation from the predicted values. For the carbon coated specimens the ratios from the $CaZrO_3$ phase were considerably higher than the predicted value (0.333) whereas the ratios for the $ZrO_{2(ss)}$ phase were lower than predicted.

These discrepancies were again atrributed to the background fit to the $Ca_{L_{23}}$ edge. As discussed in Section IV.1 the background extrapolation is carried out assuming that the background intensity falls according to $A.E^{-r}$. For a smoothly falling background (such as that prior to the O_K edge) this is a valid assumption and gives an accurate background extrapolation. However, for the $CaZrO_3$ phase in a carbon coated specimen, the background to the Ca edge was fit to the C edge. The resulting extrapolation tended to underestimate the background intensity under the Ca edge, thus overestimating the counts in the Ca edge and increasing

the $^{Ca}/_{O}$ ratio. This implies that when the background intensity is largely due to the tail of an edge at a lower energy loss, the background cannot be accurately extrapolated using the form $A.E^{-r}$.

In the $CaZrO_3$ phase the $Zr_{M_{23}}$ edge was so small that it had little effect on the background extrapolation. In the $ZrO_{2(ss)}$ phase, however, the $Zr_{M_{23}}$ edge was considerably larger and made a significant contribution to the background extrapolation. In this case the extrapolation, modified by the $Zr_{M_{23}}$ edge, tended to overestimate the background intensity under the $Ca_{L_{23}}$ edge causing a decrease in the $^{Ca}/_{O}$ ratio.

The $^{Ca}/_{O}$ ratios for the $CaZrO_3$ phase in Al coated specimens agreed closely with the predicted value, especially when a small value of Δ was used. Observations of the background extrapolation to the $Ca_{L_{23}}$ edge, however, showed the extrapolation to be extremely inaccurate. Furthermore, when EELS was used to analyze a thin Al film which was deposited and maintained under the same conditions as the Al coating, a small O_K edge was observed, Figure 41. This implied that the Al coating had probably oxidized and so any analysis for oxygen in the specimen would include a contribution from the oxidized coating and give rise to errors in the $^{Ca}/_{O}$ ratio. Thus all the $^{Ca}/_{O}$ ratios determined from the Al coated specimens were probably in error. When analyzing for oxygen in non-conducting materials, therefore, coating the specimen with Al is not recommended.

(iii) Evaluation of EELS Profiles

The results of the $^{Ca}/_{O}$ profiles across a lamellar interface are shown in Figures 42 and 43. Figure 42 shows the results obtained using the medium objective aperture (β = 4.86 mrads) and using two different values of Δ for the edge integration (namely 20 eV and 50 eV). Figure 43 shows the profiles across the same interface using the large objective aperture (β = 9.73 mrads) and the same two values of Δ (20eV and 50 eV). The error bars are shown for one data point in each phase only to simplify the plot.

These profiles show a distinct change in the $^{Ca}/_{O}$ ratio on passing from the $ZrO_{2(ss)}$ phase to the $CaZrO_3$ phase. In addition the $^{Ca}/_{O}$ ratio remained approximately constant in either phase over a large distance, in agreement with the predictions from the EDS data, Figure 33. The objective aperture size appeared to have little effect on the data but a systematic error was observed when using a 20 eV window for the edge integration as opposed to a 50 eV window. The exact cause of this systematic error is unknown, although it has previously been suggested[73] that the accuracy of the equations used for quantitation decrease considerably when energy windows $<$ 50 eV are used. Deviations from the predicted $^{Ca}/_{O}$ ratios were again observed and were attributed to the inaccuracies in the background fit to the $Ca_{L_{23}}$ edge, as discussed previously. Despite these discrepancies

however, these results indicate the quantitative energy loss analysis shows good sensitivity to sudden changes in composition.

(iv) Errors in Quantitative EELS

Since EELS is a relatively new technique there are still many problems associated with the quantitation which give rise to errors in the analyses and which are often difficult to quantify. In this work the only source of error which could be accurately quantified was that due to the counting statistics, long dwell times and relatively large energy windows were used and these errors were, therefore small, typically of the order 3-4%. However, the spectra analyzed in this work showed deviations from the predicted values of ∿20%.

One major source of error is probably due to the errors in the calculated partial ionization cross-sections, since there is little experimental data to support such calculations. Joy [61] has suggested that the relative error for an individual $\sigma(\beta,\Delta)$ value, obtained via the SIGMAK or SIGMAL program is of the order 10-15%, but that when two such values are ratioed, (when determining $^{Ca}/_{O}$ ratios, for example) the resulting error is predicted to be lower. Thus, the 10% relative error for $\sigma(\beta,\Delta)$ used in this work was, therefore, probably an overestimate.

A major factor which should not be overlooked when assessing the accuracy of EELS quantitation, obtained using a sample of known composition, is the validity of the assumption that the

composition of the sample is known. In this work for example, the $CaZrO_3$ phase was assumed to be stoichiometric. Based on this assumption, a k factor for the Ca-Zr system was determined. The composition of the $ZrO_{2(ss)}$ phase was then determined using this experimental k factor. In addition, the $^{Ca}/_{O}$ ratios were also predicted based on the assumption that the $CaZrO_3$ phase was stoichiometric. Since many systems undergo mass loss under a high energy electron beam there was no simple means of testing the validity of this assumption, especially in the chamber of the microscope. However, there was no visual evidence to suggest that differential mass loss was occurring in this system.

V. CONCLUSIONS

The major conclusions from this work may be summarized as follows:

(1) Determination of a $\phi(\rho t)$ curve for Ni at 120 kV gave values of unity for $\phi(\rho t)$ for foil thicknesses up to 80 nm but for thicker foils $\phi(\rho t)$ increased to a value of 1.3 for a foil thickness of 380 nm. This indicates that the assumption that $\phi(\rho t)$ is always equal to unity for thin foils is not necessarily a valid one, and its use may give rise to errors when corrections for x-ray absorption are required.

(2) A discrepancy of 20% was observed between the $\phi(\rho t)$ values determined in this investigation and those obtained from Monte Carlo calculations, for the same conditions. Monte Carlo calculations indicated only a 10% increase in $\phi(\rho t)$ over the 0-380 nm thickness range.

(3) The experimental technique used to determine $\phi(\rho t)$ curves in this work was suitable only for measurements at accelerating voltages $\geqslant$100 kV. At lower electron energies back-scatter became a significant problem.

(4) Thickness measurements using the contamination spot method were shown to overestimate considerably the true foil thickness. The discrepancy between contamination spot measurements and those measured by a highly accurate independent tech-

nique (Tolansky Interferometry) was always $>50\%$ and was greatest for foils $\lesssim 100$ nm in thickness. These errors have been attributed to the difficulties associated with measuring the contamination spot separation distance, since the true base of the cone of contamination is often invisible. Thus, this work indicates that, where possible, other techniques should be used when an accurate measure of the foil thickness is required.

(5) $^{Ca}/_{O}$ ratios determined by EELS for both phases of a directionally solidified eutectic, $CaZrO_3/ZrO_{2(ss)}$ showed good agreement with the values predicted from stoichiometry. The systematic deviations from the predicted ratios were attributed to problems associated with fitting the background to the $Ca_{L_{23}}$ edge, which was complicated by the presence of the C_K and $Zr_{M_{23}}$ edges.

(6) $^{Ca}/_{O}$ ratios obtained using the currently available quantitation technique were shown to be independent of the spectrometer acceptance angle (β) but systematic variations were observed when using a 20 eV edge window rather than a 50 eV window.

(7) For the ZrO_2-CaO system, the use of 4.86 mrad spectrometer acceptance angle (corresponding to the 50 μm objective aperture) as opposed to a 9.73 mrad angle (100 μm aperture) gave an improved edge signal above the background intensity.

(8) Carbon coating of the specimen, to prevent it from

charging in the microscope, was shown to be preferable to Al coating, for the purpose of EELS analysis. In the latter case, the Al edge masked much of the edge information from the specimen and in addition, the Al coating was susceptible to oxidation, giving rise to erroneous values when analyzing for oxygen.

(9) EELS Profiles across a lamellar interface showed little variation in the $^{Ca}/O$ ratio within each phase (in agreement with EDS data) but showed a sharp discontinuity in the $^{Ca}/O$ ratio at the interface. This indicates that energy loss analysis shows good sensitivity to sudden changes in composition.

(10) This investigation indicates that quantitative energy loss analysis of a multicomponent system is considerably complicated by the presence of extra edges in the spectrum which contribute to the intensity of edges at higher energy losses. Extreme caution should, therefore, be exercized when interpreting results from a multicomponent system of unknown composition, since the errors associated with such an analysis are often peculiar to the system of interest. Such analyses could be greatly improved by the incorporation of an accurate edge-stripping routine in the quantitation program.

TABLE I

Specimen Thicknesses for $\varphi(\rho t)$ Determinations

Cu thickness (nm)	Ni thickness (nm)	ρt(mg cm^{-2}) for Ni
59 ± 5	25.0 ± 5	0.022
"	55.0 ± 5	0.049
"	80.0 ± 5	0.072
"	110.0 ± 5	0.099
"	167.5 ± 5	0.150
"	200.0 ± 5	0.179
"	260.0 ± 5	0.233
"	310.0 ± 5	0.278
"	380.0 ± 5	0.341

TABLE II

Comparison of Techniques for Thin Foil Thickness Measurements

Quartz Oscillator (nm)	Talysurf $\pm$ 10 nm	Tolansky Interferometer $\pm$ 5 nm
100.8	110.0	107.1
188.6	200.0	186.8
350.3	380.0	368.7

TABLE III

Variation of $\phi(\rho o)$ with Accelerating Voltage at 380 nm

Accelerating Voltage		Analytical Sensitivity (Eqn. 5)
120 kV	1.030 ± 0.064	X
100 kV	1.023 ± 0.046	X
80 kV	1.183 ± 0.051	✓
60 kV	1.293 ± 0.051	✓

TABLE IV

Comparison of Thin Foil Thickness Measurements

Film	Thickness (Tolansky)	Thickness (Contamination spots)	Discrepancy
Al	117 ± 5 nm	190 ± 31 nm	62%
Al	177 ± 5 nm	270 ± 40 nm	54%
Cu	59 ± 5 nm	170 ± 33 nm	189%

TABLE V

Relationship Between Objective Aperture Diameter and Spectrometer Acceptance Angle (β)

Objective Aperture Diameter	Spectrometer Acceptance Angle (β)
100 μm	9.73 mrad
50 μm	4.86 mrad
20 μm	1.95 mrad

TABLE VI

Operating and Analysis Parameters Used for the Evaluation of $^{Ca}/_{O}$ Atomic Ratios

	Coating	β	Δ edge	Δ background
1.	C	9.73 mrad	20 eV	40 eV
2.	C	9.73 mrad	50 eV	50 eV
3.	C	4.86 mrad	20 eV	40 eV
4.	C	4.86 mrad	50 eV	50 eV
5.	Al	9.73 mrad	20 eV	40 eV
6.	Al	9.73 mrad	50 eV	50 eV
7.	Al	4.86 mrad	20 eV	40 eV
8.	Al	4.86 mrad	50 eV	50 eV

TABLE VII

σ (β, Δ) for the Oxygen K Shell at 120 kV

Δ (eV)	σ (β = 9.73 mrads)	σ (β = 4.86 mrads)
10	1.8184×10^{-22}	9.5995×10^{-23}
20	3.4996×10^{-22}	1.8405×10^{-22}
30	5.0559×10^{-22}	2.6493×10^{-22}
40	6.4979×10^{-22}	3.3930×10^{-22}
50	7.8358×10^{-22}	4.0777×10^{-22}
60	9.0781×10^{-22}	4.7088×10^{-22}
70	1.0233×10^{-21}	5.2911×10^{-22}
80	1.1308×10^{-21}	5.8290×10^{-22}
90	1.2309×10^{-21}	6.3263×10^{-22}

TABLE VIII

$\sigma(\beta,\Delta)$ for the Calcium L Shell at 120 kV

Δ(eV)	σ (β = 9.73 mrad)	σ (β = 4.96 mrad)
10	1.1303×10^{-21}	7.2690×10^{-22}
20	2.2983×10^{-21}	1.4695×10^{-21}
30	3.3891×10^{-21}	2.1549×10^{-21}
40	4.3948×10^{-21}	2.7799×10^{-21}
50	5.3178×10^{-21}	3.3471×10^{-21}
60	6.1631×10^{-21}	3.8609×10^{-21}
70	6.9367×10^{-21}	4.3261×10^{-21}
80	7.6448×10^{-21}	4.7475×10^{-21}
90	8.2931×10^{-21}	5.1294×10^{-21}

TABLE IX

Operating and Analysis Parameters Used for EELS Profiles

Profile #	Coating	β (mrads)	Δ edge	Δ background
1	C	4.86	20 eV	50 eV
2	C	4.86	50 eV	50 eV
3	C	9.73	20 eV	20 eV
4	C	9.73	50 eV	50 eV

TABLE X

Comparison of Experimentally Determined $^{Ca}/_{O}$ Ratios Under Different Analysis Conditions

	Coating	β (mrads)	Δ edge (eV)	Δ bgd (eV)	$^{Ca}/_{O}{}_{CaZrO_3}$	$^{Ca}/_{O}{}_{ZrO_{2(ss)}}$
1	C	9.73	20	40	0.392 ± 0.012	0.077 ± 0.006
2	C	9.73	50	50	0.401 ± 0.007	0.080 ± 0.017
3	C	4.86	20	40	0.394 ± 0.018	0.097 ± 0.007
4	C	4.86	50	50	0.401 ± 0.018	0.075 ± 0.017
5	Al	9.73	20	40	0.336 ± 0.024	0.077 ± 0.006
6	Al	9.73	50	50	0.252 ± 0.034	0.013 ± 0.005
7	Al	4.86	20	40	0.341 ± 0.023	0.060 ± 0.007
8	Al	4.86	50	50	0.252 ± 0.017	0.014 ± 0.002

TABLE X

Comparison of Experimentally Determined $^{Ca}/_{O}$ Ratios Under Different Analysis Conditions

	Coating	β (mrads)	Δ edge (eV)	Δ bgd (eV)	$^{Ca}/_{O}$ $_{CaZrO_3}$	$^{Ca}/_{O}$ $_{ZrO_{2}(ss)}$
1	C	9.73	20	40	0.392 ± 0.012	0.077 ± 0.006
2	C	9.73	50	50	0.401 ± 0.007	0.080 ± 0.017
3	C	4.86	20	40	0.394 ± 0.018	0.097 ± 0.007
4	C	4.86	50	50	0.401 ± 0.018	0.075 ± 0.017
5	Al	9.73	20	40	0.336 ± 0.024	0.077 ± 0.006
6	Al	9.73	50	50	0.252 ± 0.034	0.013 ± 0.005
7	Al	4.86	20	40	0.341 ± 0.023	0.060 ± 0.007
8	Al	4.86	50	50	0.252 ± 0.017	0.014 ± 0.002

TABLE XI

Effect of Objective Aperture Size on $^{Ca}/_{O}$ Ratio

(Carbon-coated Specimens)

Phase	$^{Ca}/_{O}$ (β = 4.86 mrads)	$^{Ca}/_{O}$ (β = 9.73 mrads)
$CaZrO_3$	0.394 ± 0.018	0.392 ± 0.012
$CaZrO_3$	0.401 ± 0.018	0.401 ± 0.007
$ZrO_{2(ss)}$	0.097 ± 0.007	0.077 ± 0.006
$ZrO_{2(ss)}$	0.075 ± 0.017	0.080 ± 0.017

TABLE XII

Effect of Energy Window, Δ, on $^{Ca}/_{O}$ Ratio

(Carbon-coated Specimens)

Phase	$^{Ca}/_{O}$ Ratios Δ edge = 20 eV Δ bgd = 40 eV	 Δ edge = 50 eV Δ bgd = 50 eV
$CaZrO_3$	0.392 ± 0.012	0.401 ± 0.007
$ZrO_{2(ss)}$	0.077 ± 0.006	0.080 ± 0.017
$CaZrO_3$	0.336 ± 0.024	0.252 ± 0.034
$ZrO_{2(ss)}$	0.077 ± 0.006	0.013 ± 0.005

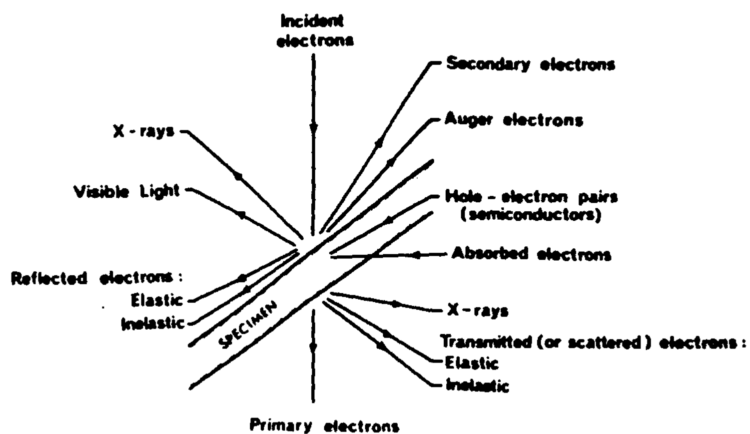

Figure 1 - Signals generated as a result of the interaction of an electron beam and a thin specimen. [From Joy and Maher [1]]

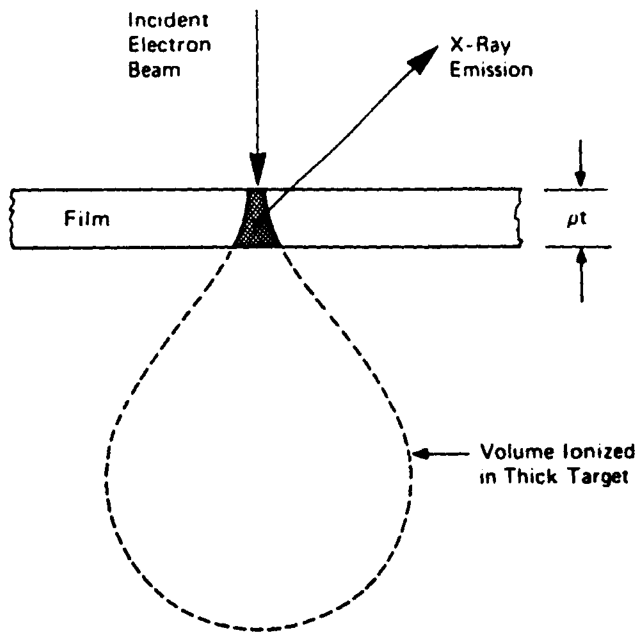

Figure 2 - The x-ray emission volume in a thick target relative to that in a thin foil.

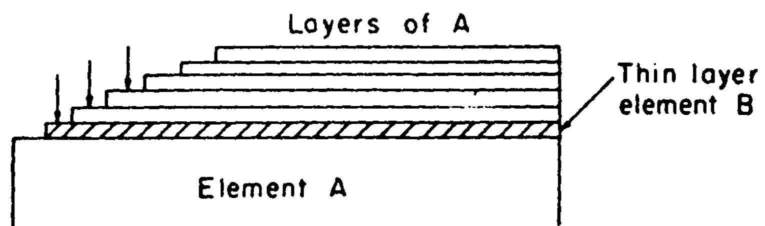

Figure 3 - Sandwich sample used to measure $\phi(\rho t)$.

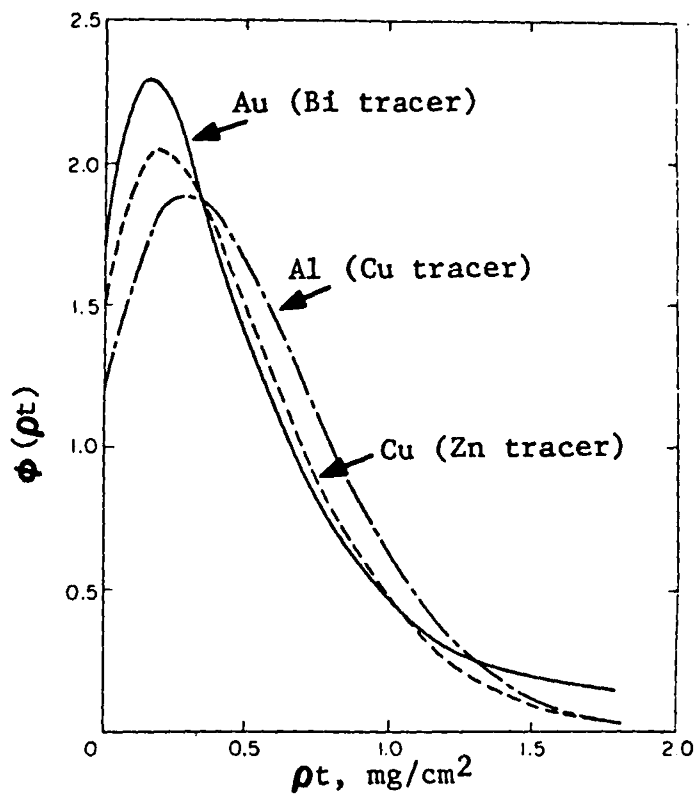

Figure 4 - The $\phi(\rho t)$ curves of Castaing and Deschamps [16] measured at 29 kV.

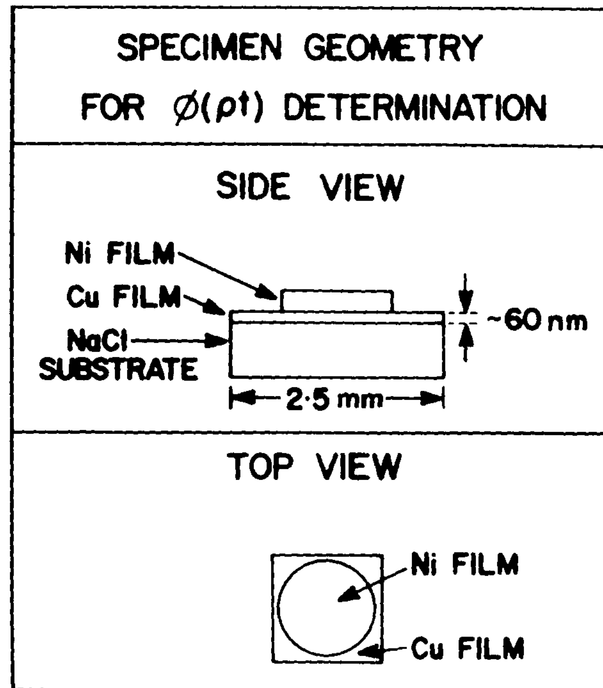

Figure 5 - Specimen geometry used in determination of $\phi(\rho t)$. Thicknesses of Ni varying from ∿25 to 380 nm were deposited on top of the Cu film leaving portions exposed.

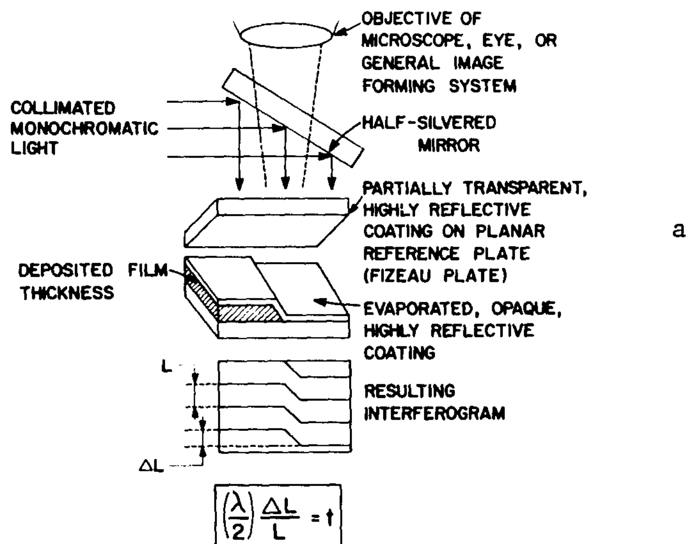

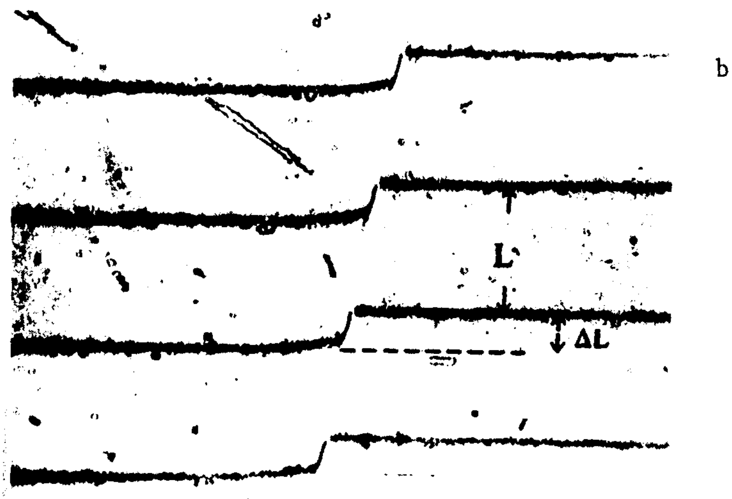

Figure 6 - (a) Schematic: principles of Tolansky interferometry (b) Typical interferogram.

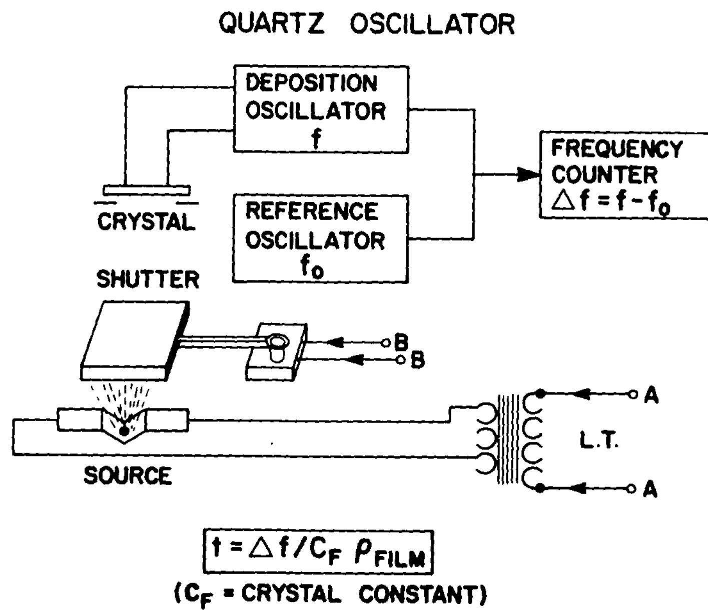

Figure 7 - Schematic: measurement of thickness of deposited film of density ρ by determining frequency shift (Δf) of quartz oscillator.

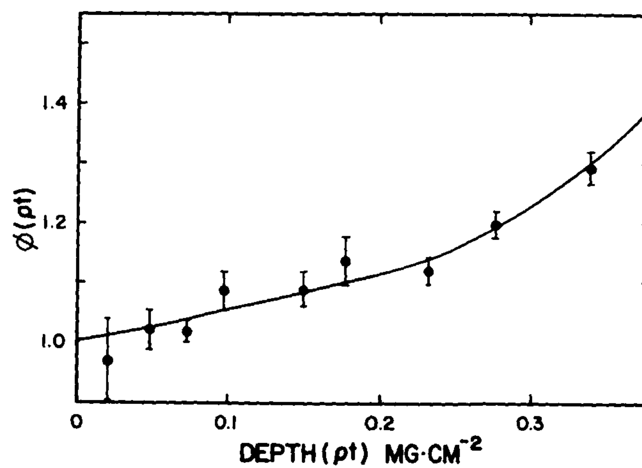

Figure 8 -Experimental data showing increase in $\phi(\rho t)$ with mass thickness for thin films of Ni upto 380 nm thick using 120 kV electrons.

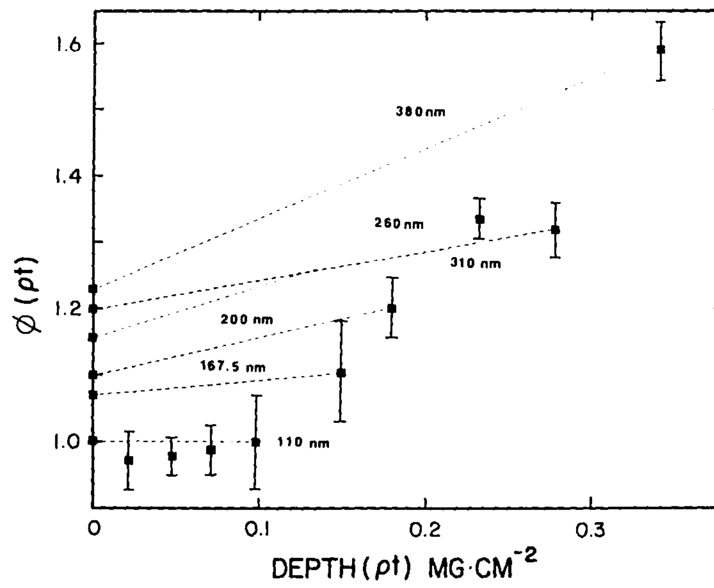

Figure 9 - Experimental $\phi(\rho t)$ data for thin films of Ni up to 380 nm thick, at 60kV.

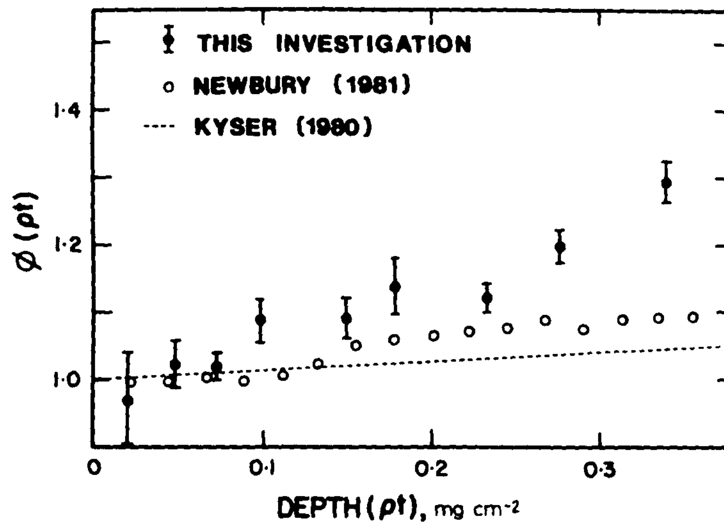

Figure 10 - Comparison of experimental data from present investigation with Monte Carlo calculations. (Work of Newbury is for Ni at 120 kV, while data of Kyser is for Cu at 100 kV.)

Figure 11 - Contamination spots created on upper and lower surface of an Al foil.

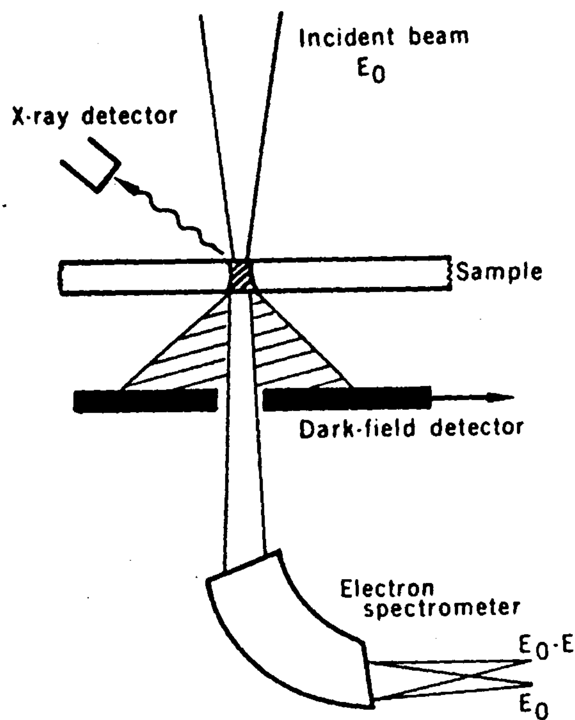

Figure 12 - Schematic illustration of a combined electron microscope and microanalytical facility. The incident beam is focused to a spot on the thin sample and either x-ray or energy loss spectra can be collected for microanalysis. [from Joy and Maher (30).]

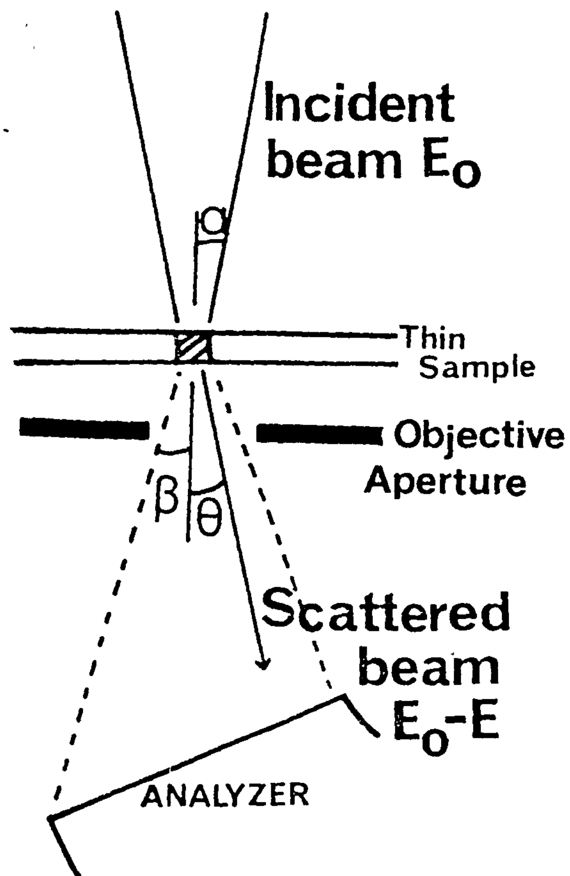

Figure 13 - The geometry of energy loss spectroscopy in the electron microscope, showing the scattering angle θ, the spectrometer acceptance angle β and the incident beam convergence angle α. [from Joy (32)]

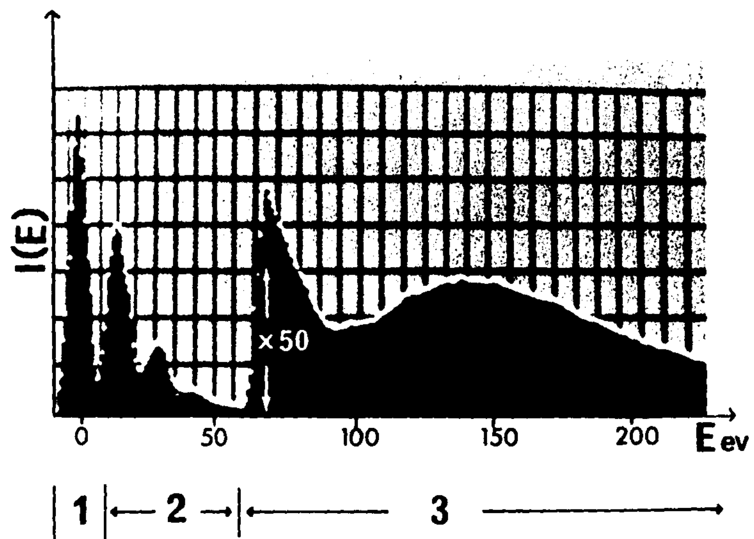

Figure 14 - Typical ELS spectra from Si at 100 kV showing the zero loss peak , the plasmon peaks and a gain change of 50 followed by the Si_{L23} edge. [from Joy [32]]

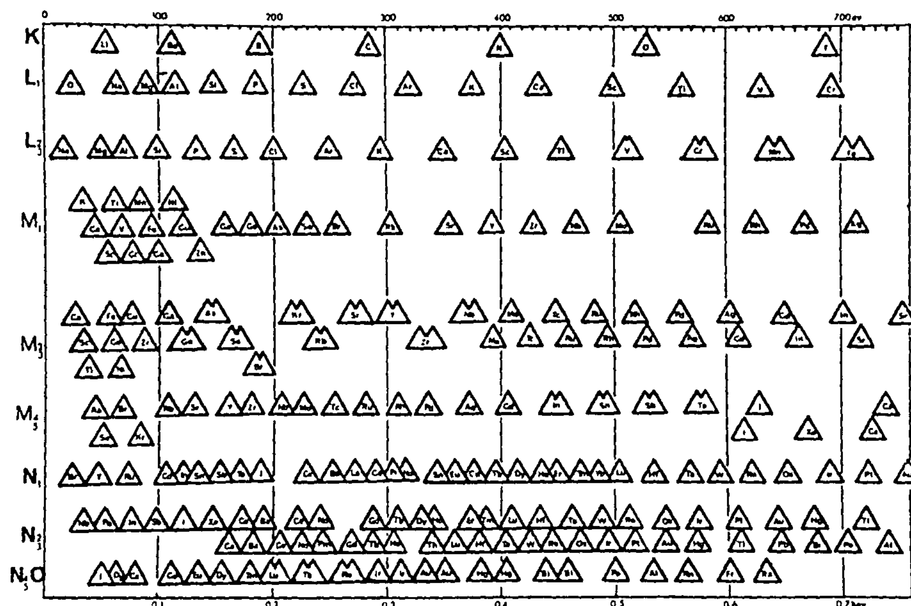

Figure 15 - Position of ionization edges in energy loss range 0-700 eV. [From Joy and Maher(34)]

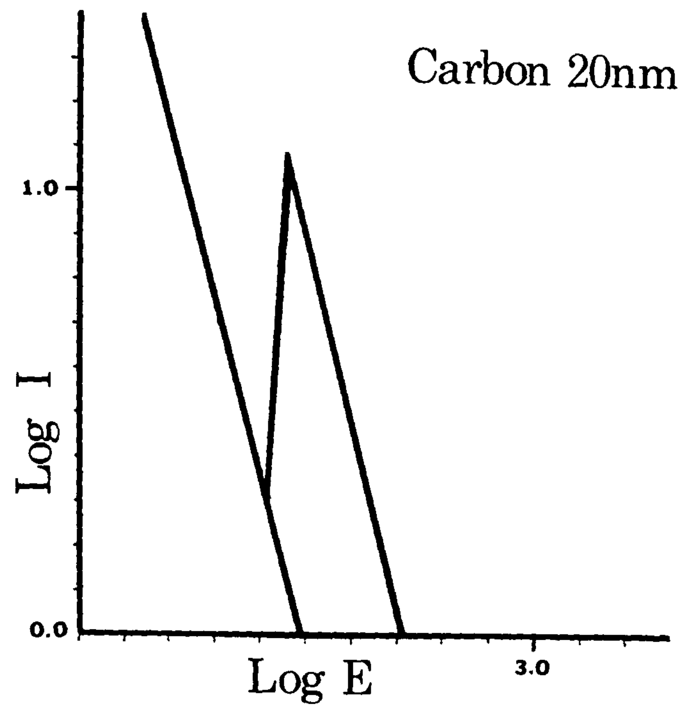

Figure 16 - Log-log plot of an energy-loss spectrum showing subtraction of background intensity. [After Egerton and Whelan(35)]

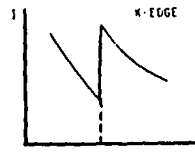

(a)

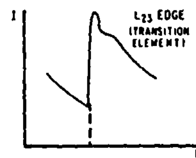

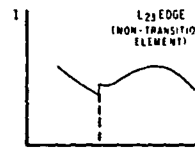

(b)

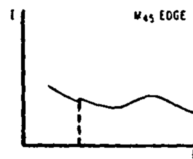

(c)

Figure 17 - (a) Typical shape of a K ionization edge. (b) Typical shapes of L_{23} ionization edges. (c) Typical shape of an M_{45} edge. [After Menzies and Bricknell[37]]

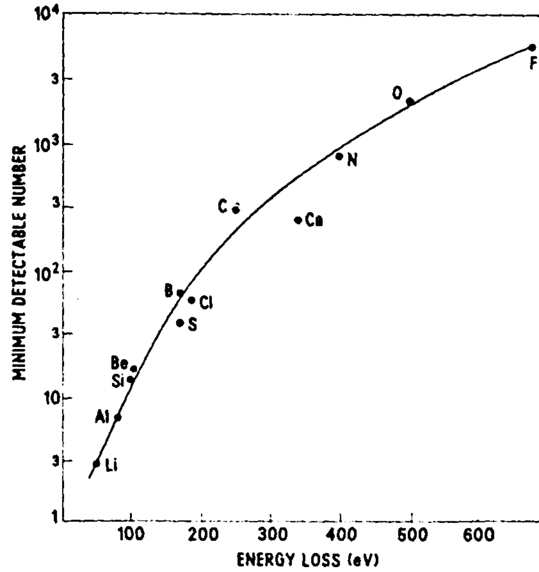

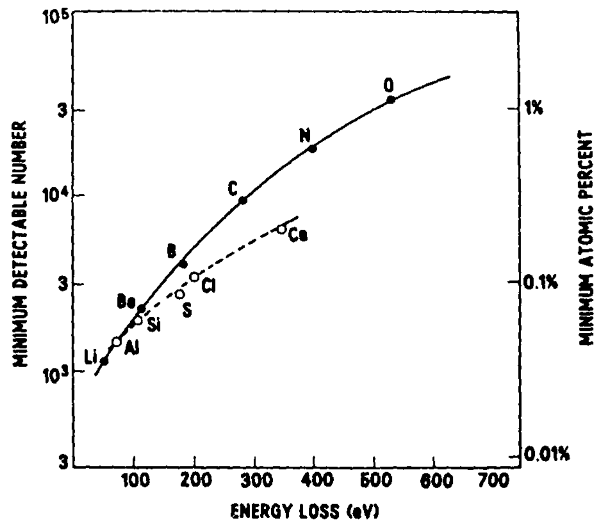

Figure 18 - (a) The calculated self-detection limits for an ELS system operating at 100 kV with an acceptance angle of 3 mrad. (b) Minimum detectable number of atoms for various elements in 50 nm thick Fe foil under the same operating conditions. [From Joy and Maher[41]]

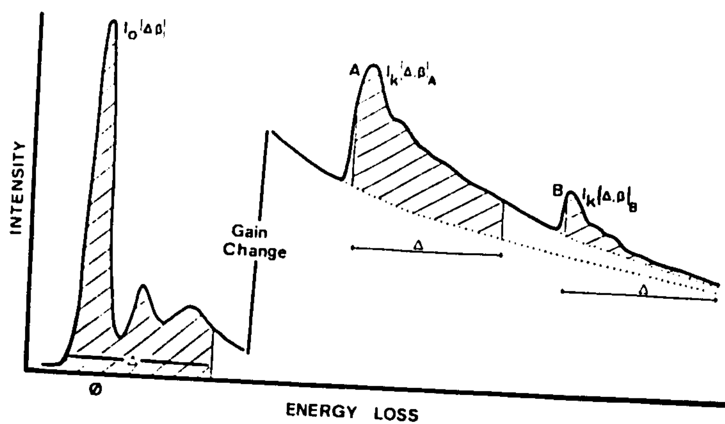

Figure 19 - Schematic illustration of an energy loss spectrum indicating the quantities required for quantitation. [From Joy and Maher(45)]

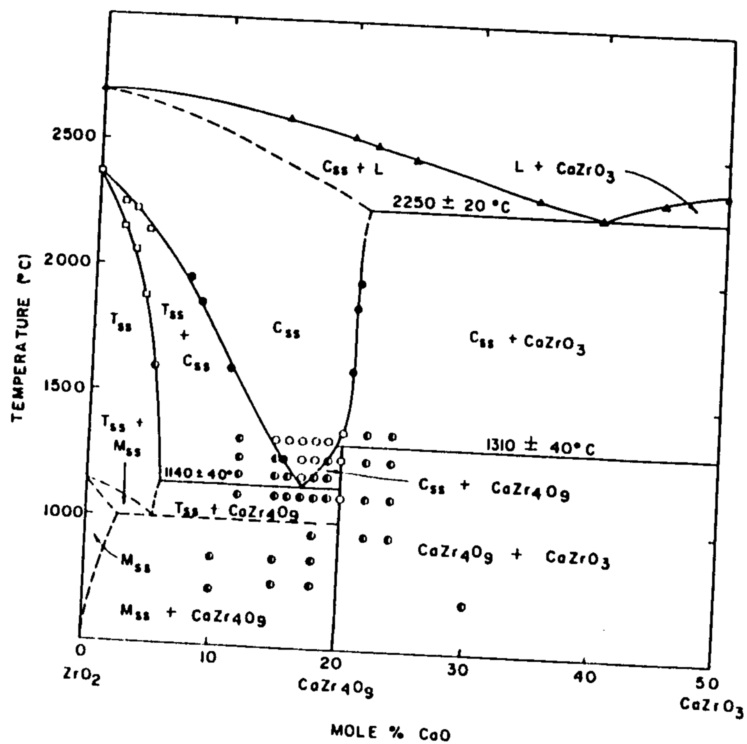

Figure 20 - ZrO_2-CaO phase diagram due to Stubican and Hellman(55).

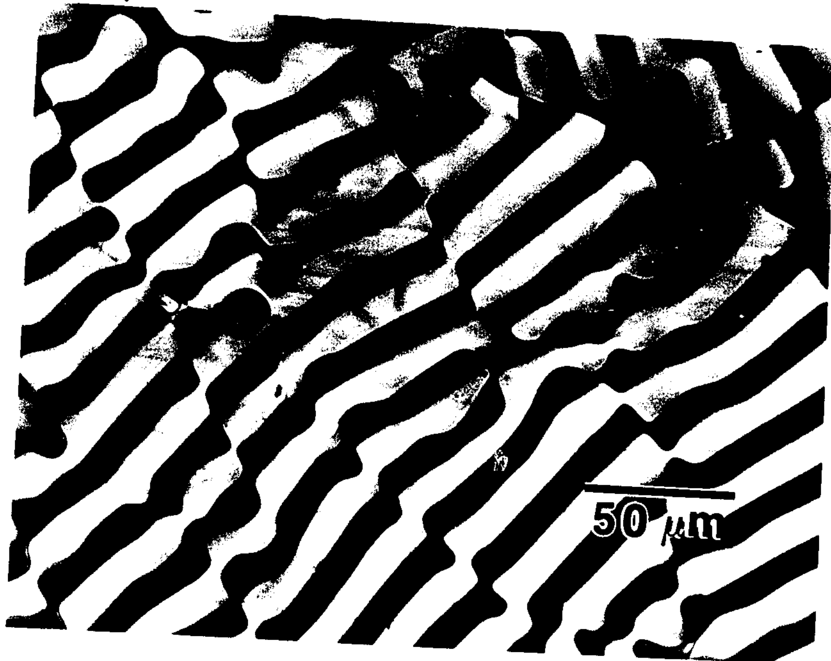

Figure 21 - Low magnification transmission optical photomicrograph of the $CaZrO_3/ZrO_2(ss)$ directionally solidified eutectic.

Figure 22 - TEM micrograph of the $CaZrO_3/ZrO_{2(ss)}$ directionally solidified eutectic.

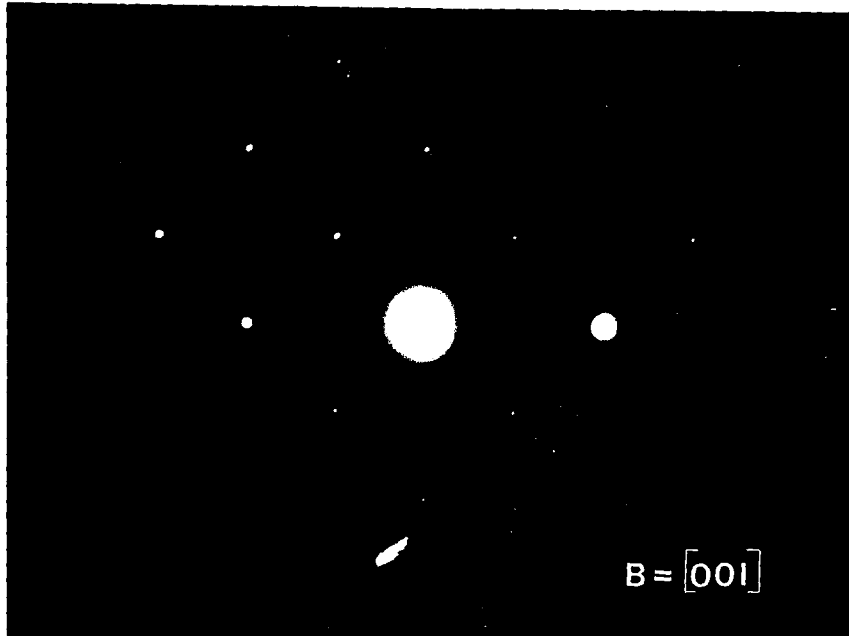

Figure 23 - [100] diffraction pattern from the $ZrO_{2(ss)}$ phase.

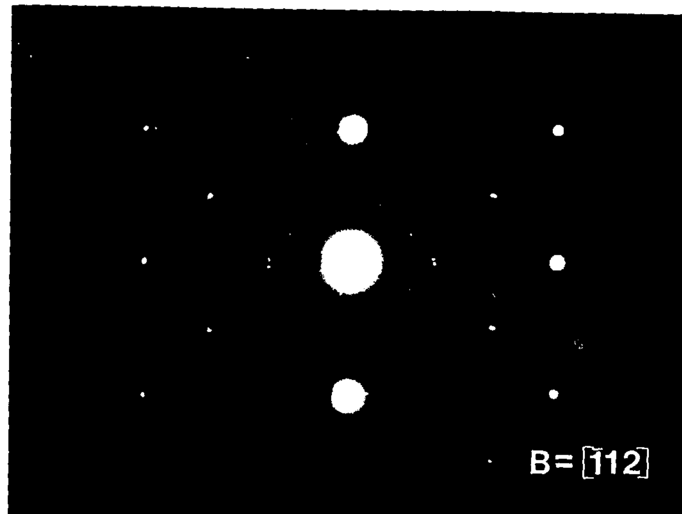

a

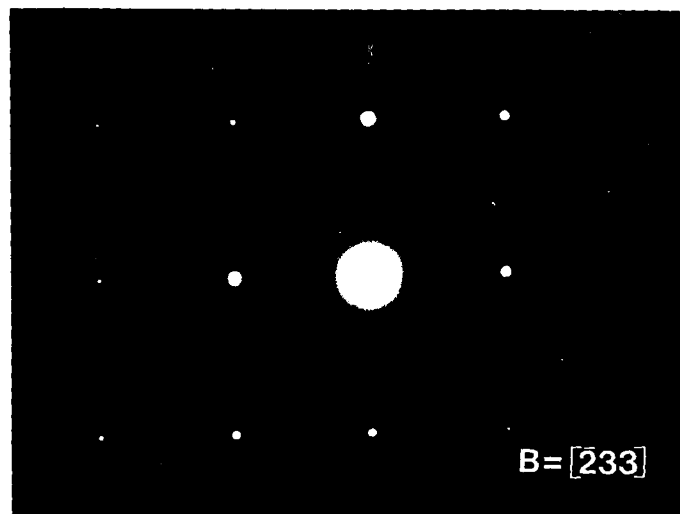

b

Figure 24 - (a) and (b) Diffraction patterns from $ZrO_{2(ss)}$ phase showing diffuse "donut" shaped features.

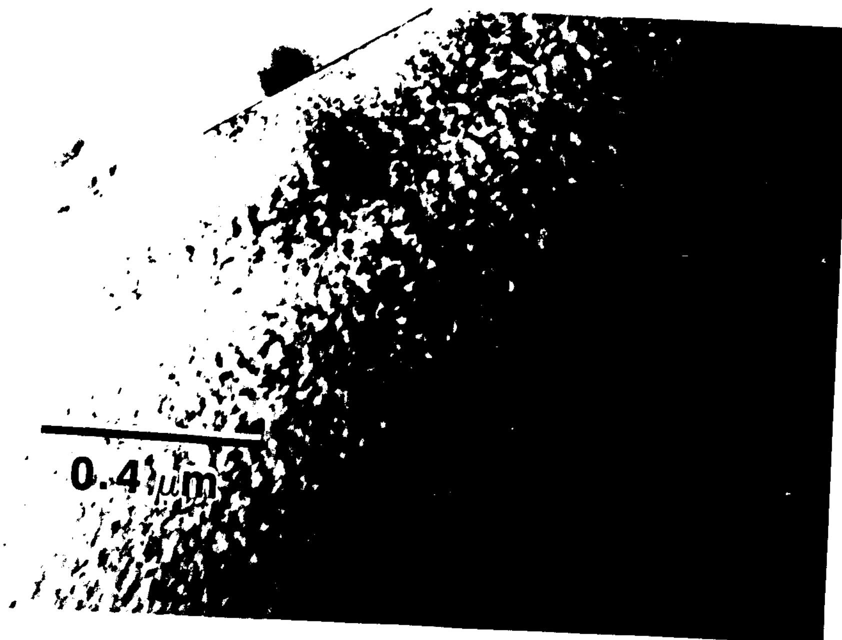

Figure 25 - Bright field micrograph of $ZrO_{2(ss)}$ phase showing mottled contrast associated with the diffuse diffraction features of Figure 24.

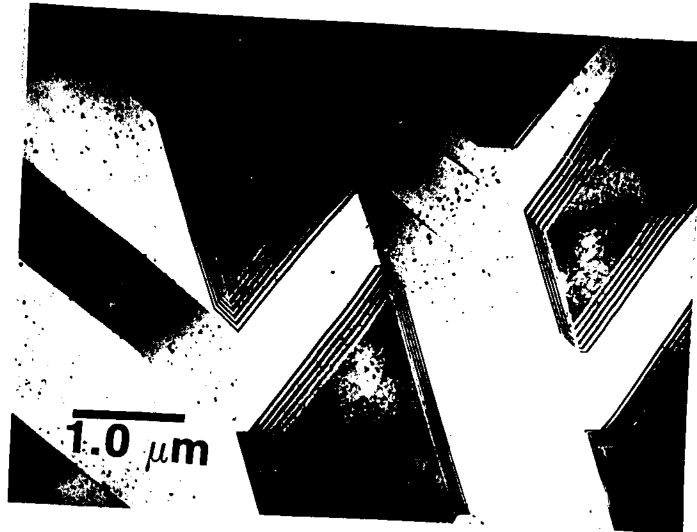

a

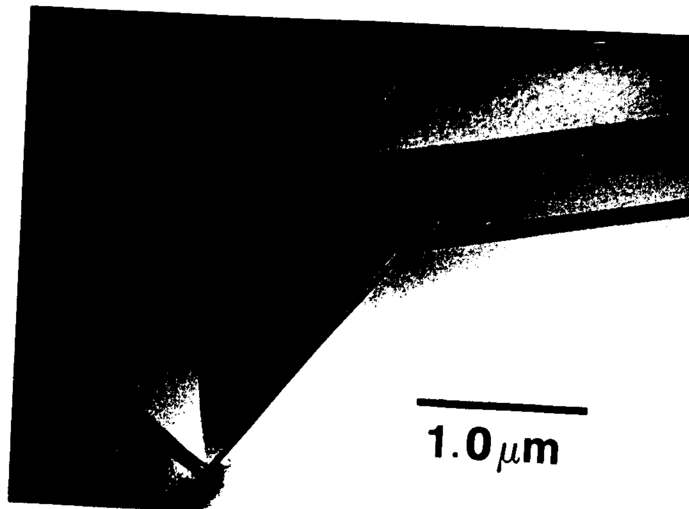

b

Figure 26 - (a) and (b) Typical boundaries observed in $CaZrO_3$ phase.

Figure 27 - Behavior of bend contours indicates presence of low angle boundaries in some areas of $CaZrO_3$ phase.

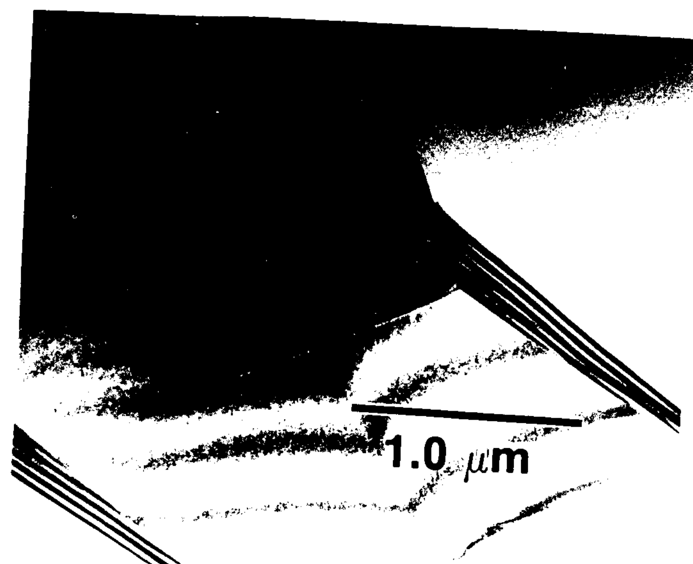

a

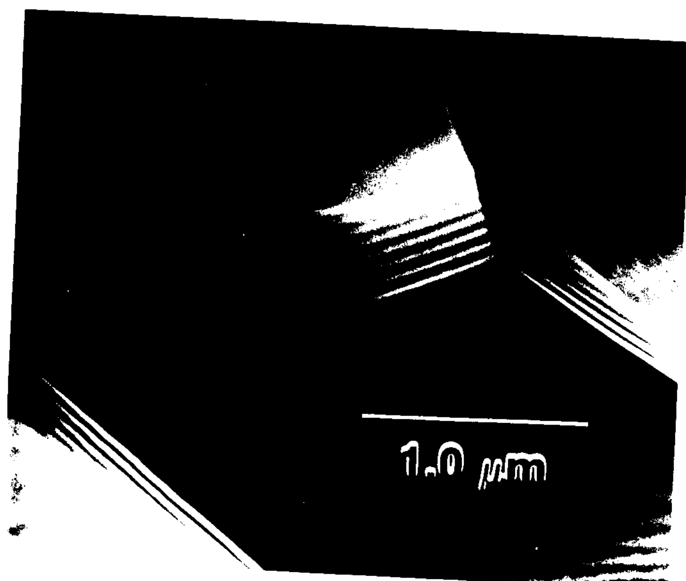

b

Figure 28 - δ boundaries in $CaZrO_3$ (a) Asymmetrical fringe contrast in bright field. (b) Symmetrical fringe contrast in dark field.

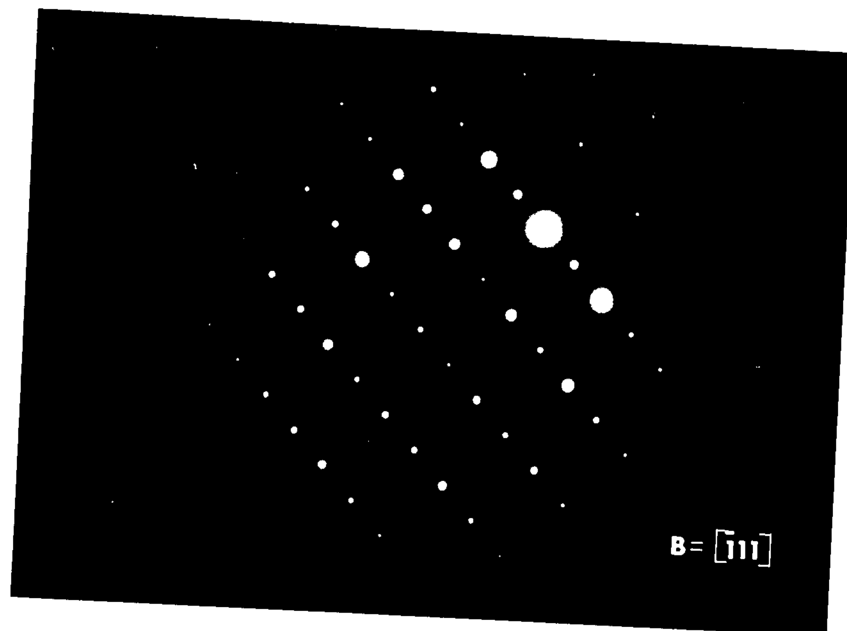

Figure 29 - Diffraction pattern from $CaZrO_3$ showing retained high temperature, ordered cubic form.

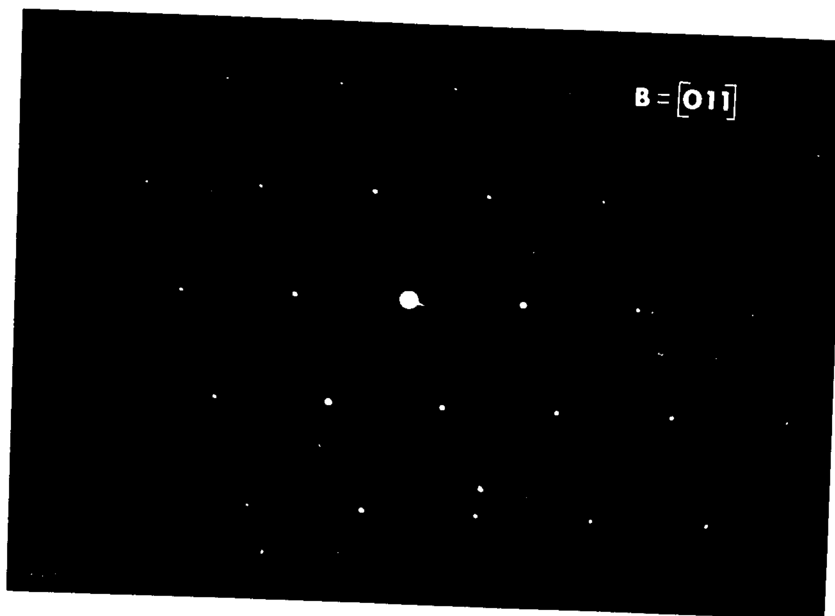

Figure 30 - Cubic diffraction pattern from $CaZrO_3$ with no evidence of extra spots due to ordering.

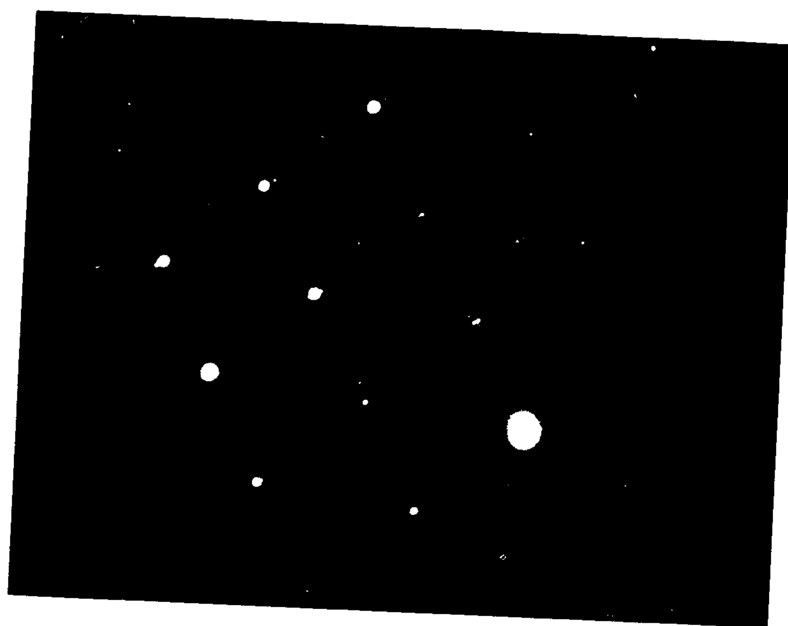

Figure 31 - Non-cubic diffraction pattern from $CaZrO_3$.

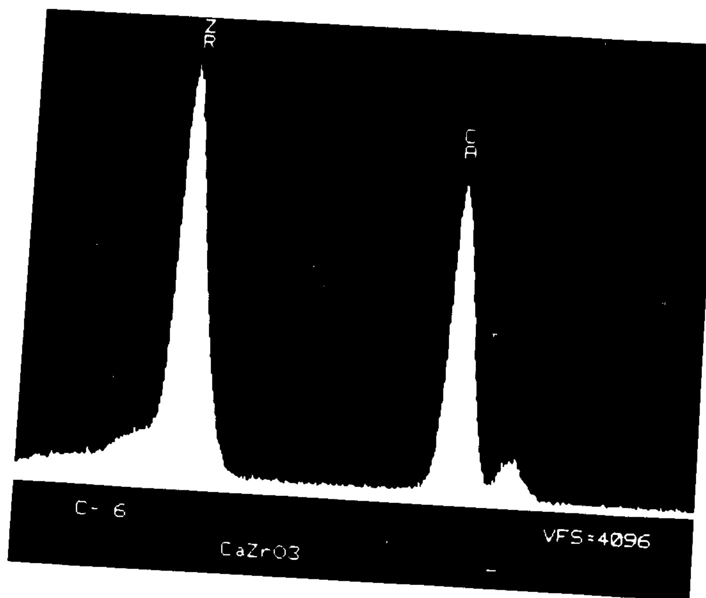

a

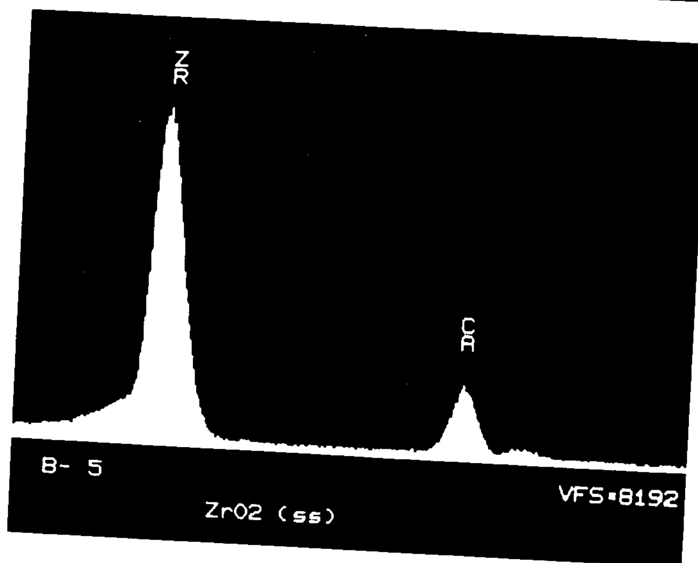

b

Figure 32 - (a) Typical EDS spectrum from $CaZrO_3$ phase. (b) Typical EDS spectrum from $ZrO_{2(ss)}$ phase.

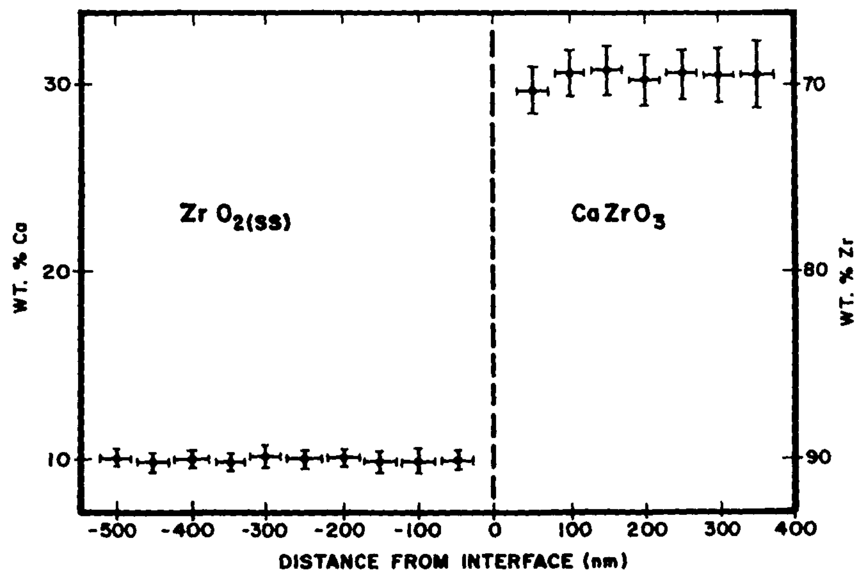

Figure 33 - EDS Profile across a lamellar interface showing no appreciable cation segregation at the boundary.

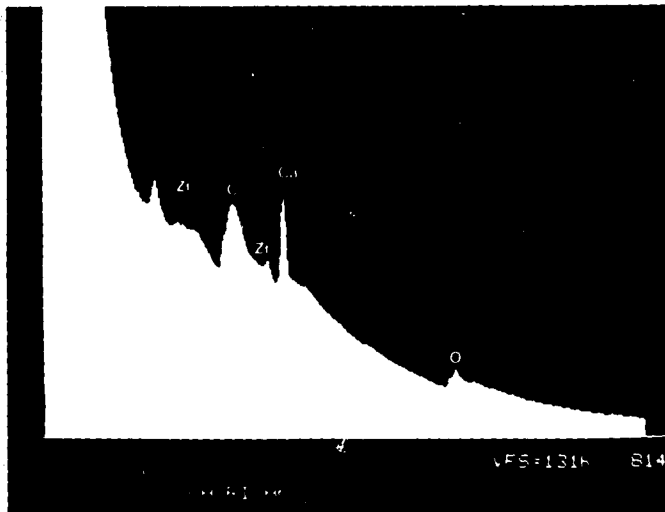

a

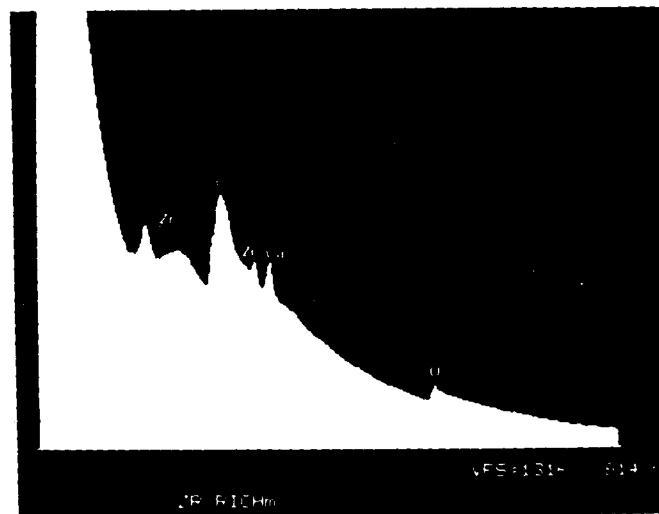

b

Figure 34 - (a) Typical EELS spectrum from $CaZrO_3$ phase. (b) Typical EELS spectrum from $ZrO_{2(ss)}$ phase.

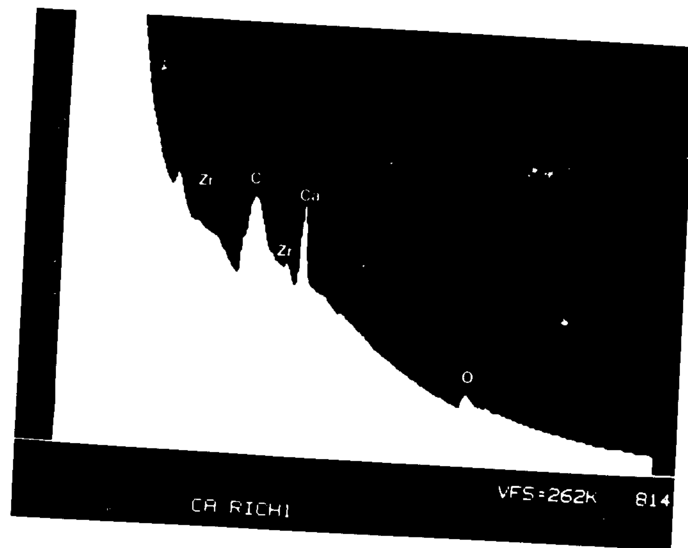

a

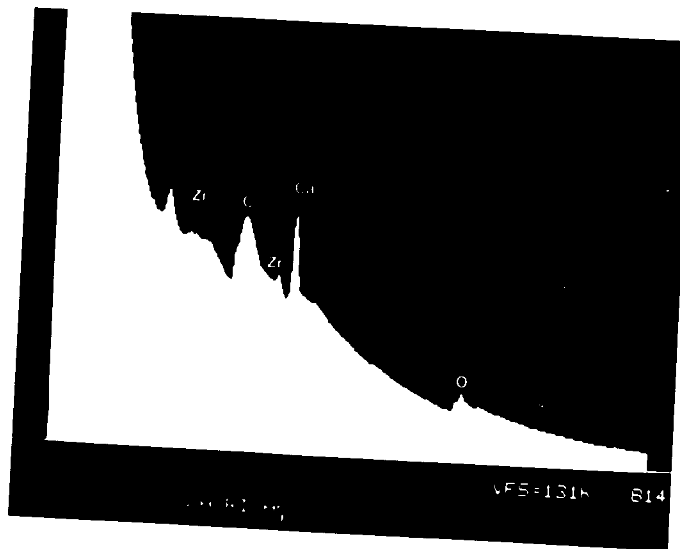

b

Figure 35 - Effect of objective aperture size on spectra from $CaZrO_3$ phase. (a) Spectrum using 100 μm aperture (β = 9.73 mrads). (b) Spectrum using 50 μm aperture (β = 4.86 mrads) showing improved edge to background signal.

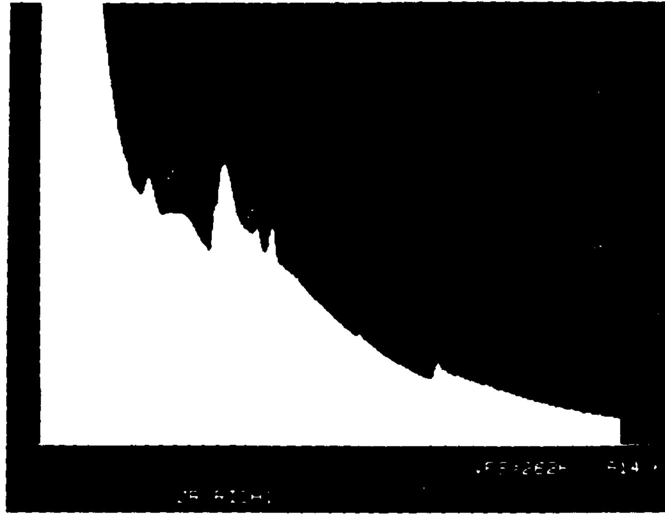

a

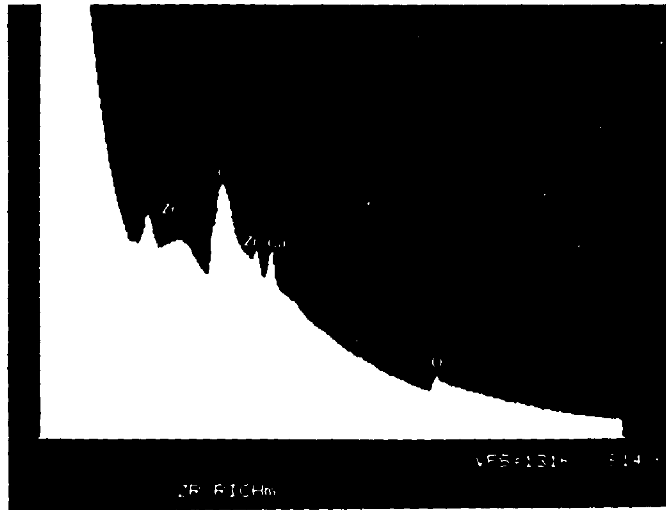

b

Figure 36 - Effect of objective aperture size on spectra from $ZrO_{2(ss)}$ phase. (a) Using 100 μm aperture (β = 9.73 mrads). (b) Using 50 μm aperture (β = 4.86 mrads).

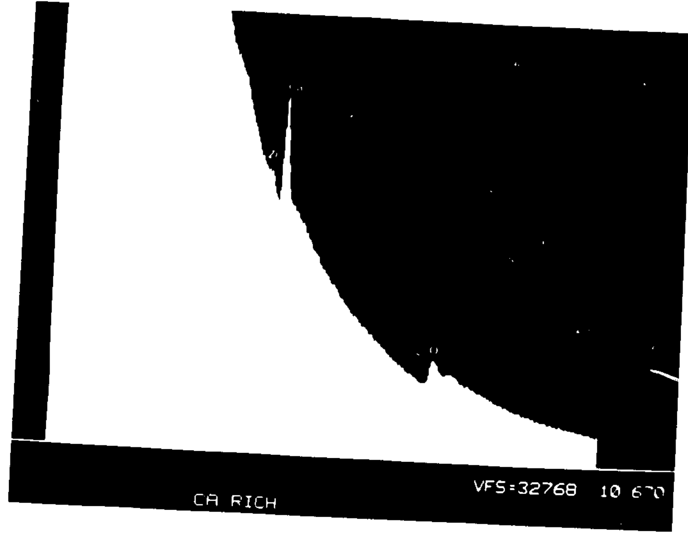

a

b

Figure 37 - Typical EELS spectra from Al coated specimen. (a) $CaZrO_3$ phase. (b) $ZrO_{2(ss)}$ phase.

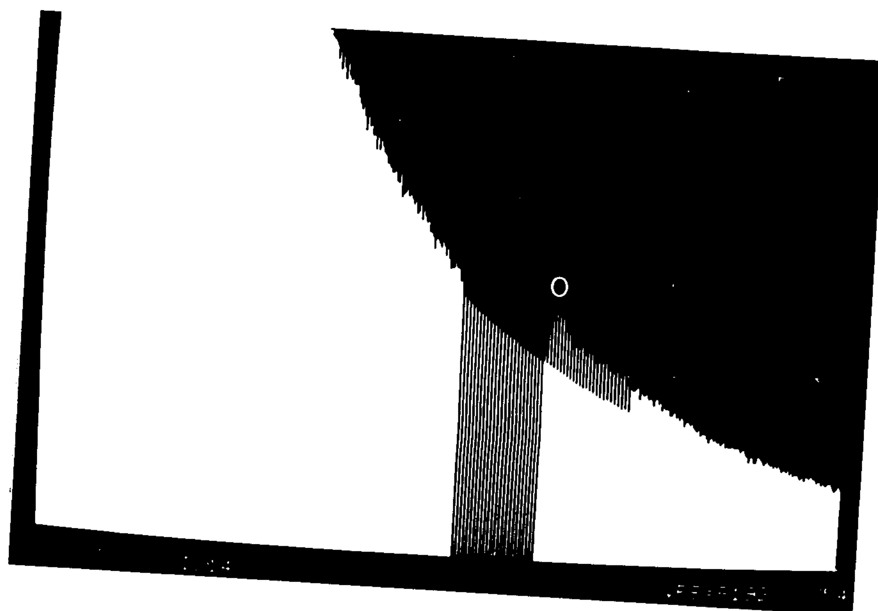

Figure 38 - Portion of EELS spectrum showing background fit to the oxygen K edge.

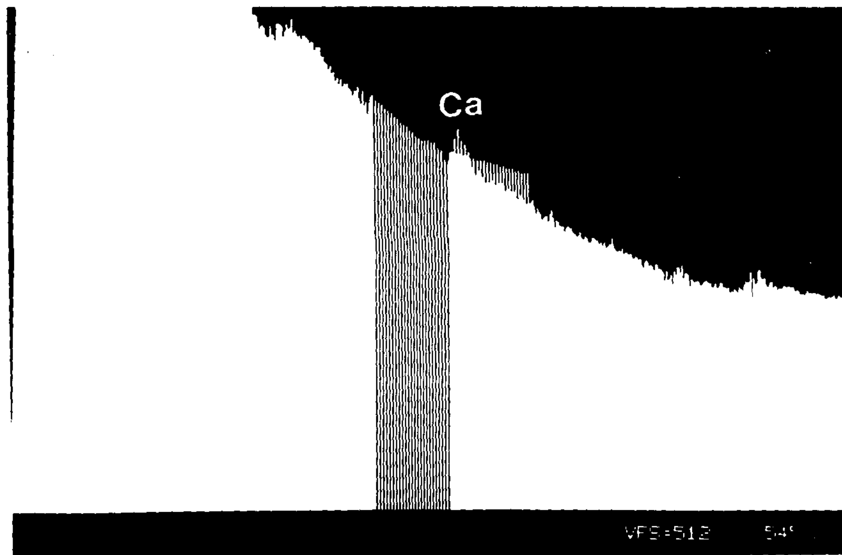

Figure 39 - Portion of EELS spectrum from Al coated specimen showing poor fit to the calcium edge.

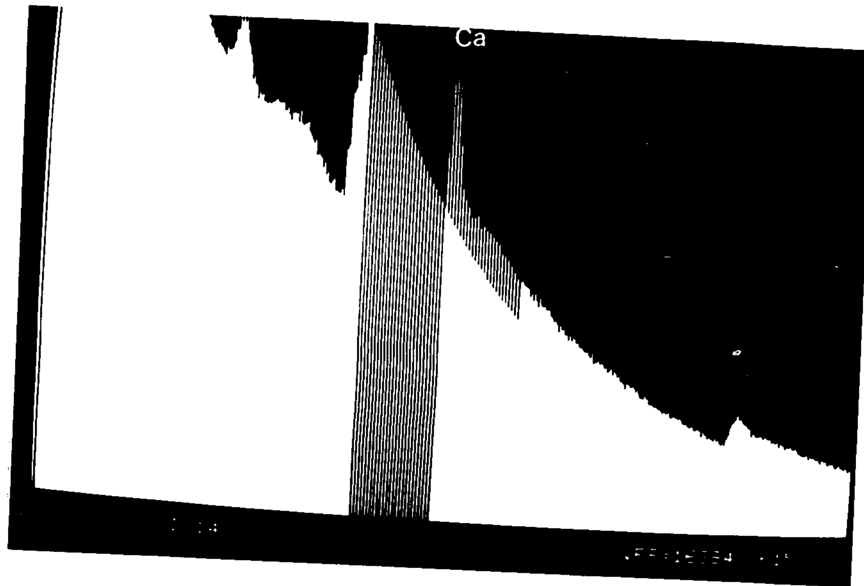

Figure 40 - Portion of EELS spectrum from C coated specimen showing a reasonable fit to the calcium edge.

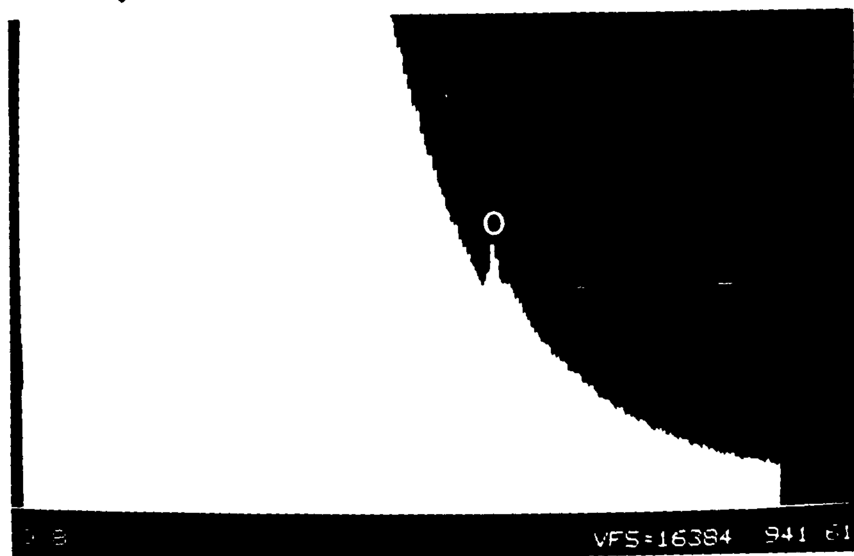

Figure 41 - Portion of EELS spectrum from an evaporated Al film maintained under the same conditions as the Al coated specimen, showing a small oxygen edge.

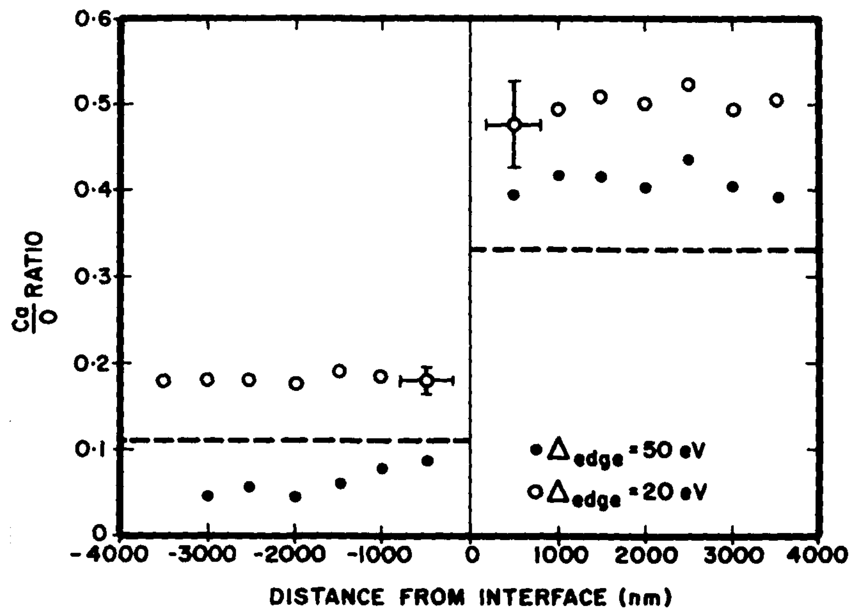

Figure 42 - $^{Ca}/_{O}$ profiles across a lamellar interface using medium objective aperture (β = 4.86 mrads) and energy windows of 20 eV and 50 eV. (Dashed lines represent the $^{Ca}/_{O}$ ratios calculated from the stoichiometry.)

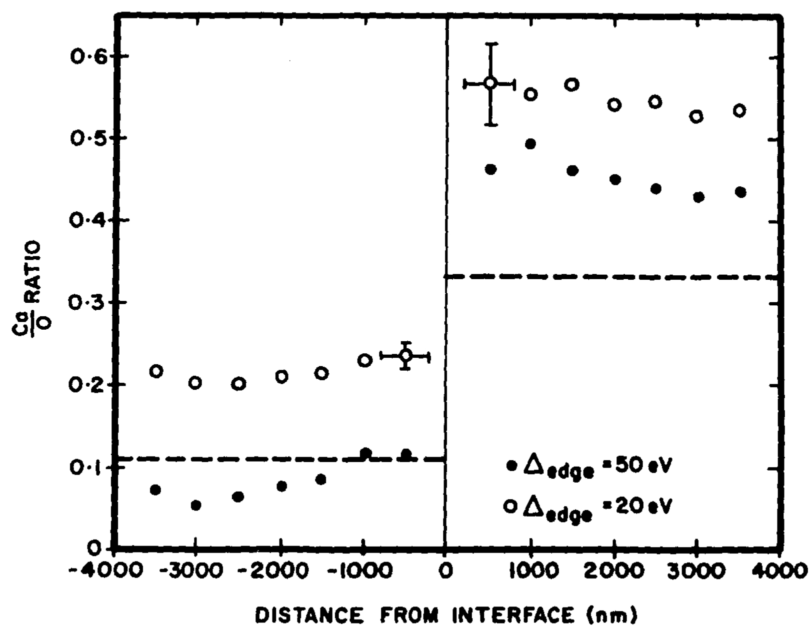

Figure 43 - $^{Ca}/_{O}$ profiles across a lamellar interface using large objective aperture (β = 9.73 mrads) and energy windows of 20 eV and 50 eV. (Dashed lines represent the $^{Ca}/_{O}$ ratios calculated from the stoichiometry.)

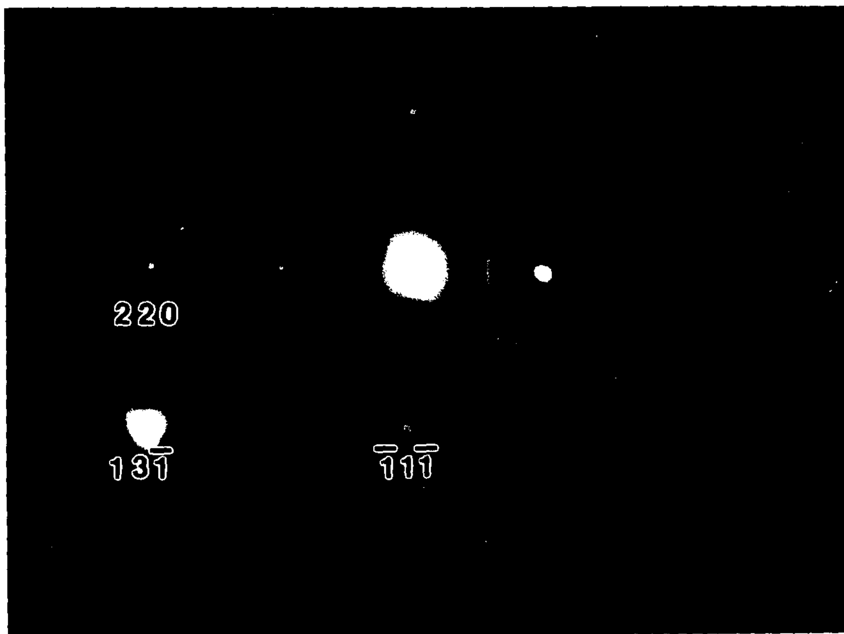

Figure 44 - Low index diffraction pattern from Al superimposed with image of objective aperture. [Courtesy S. F. Baumann]

VI. REFERENCES

1. D. M. Maher and D. C. Joy, J. Metals, Feb. 1977, 26.
2. G. Cliff and G. W. Lorimer, J. Microscopy 103 (1975) 203.
3. J. I. Goldstein, J. L. Costley, G. W. Lorimer and S. J. B. Reed, SEM 1977, ed. O. Johari, Chicago 1977, 315.
4. G. W. Lorimer, G. Cliff and J. N. Clark, Developments in Electron Microscopy and Analysis 1975, ed. J. A. Venables, London Academic Press, 1977, 153.
5. B. Bender, D. B. Williams and M. R. Notis, J. Amer. Ceram. Soc. 63 (1980) 149.
6. S. Mehta, J. I. Goldstein, D. B. Williams and A. D. Romig, Microbeam Analysis 1979, ed. D. E. Newbury, San Francisco Press, 119.
7. R. Tixier and J. Philibert, Proc. 5th Int. Cong. on X-ray Optics and Microanalysis, eds. G. Mollenstedt and K. H. Gaukler, Springer-Verlag, Berlin, 1969, 1980.
8. R. König, Electron Microscopy in Mineralogy, ed. H. R. Wenk, Springer-Verlag, Berlin, 1976, 526.
9. H. Yakowitz and D. E. Newbury, SEM 1976, ed. O. Johari, Chicago, 1976, 151.
10. R. W. Glitz, M. R. Notis, D. B. Williams and J. I. Goldstein, Microbeam Analysis 1981, ed. R. H. Geiss, San Francisco Press Inc., 309.

11. R. Castaing, Adv. Electron. Electron Phys. 13 (1960) 317.

12. A. Vignes and G. Dez, Br. J. Appl. Phys. 1 (1968) 1309.

13. R. Castaing and J. Henoc, X-ray Optics and Microanalysis, Herman, Paris, 1966, 120.

14. J. D. Brown and L. Parobek, Adv. X-ray Analysis, 16 (19/3) 198.

15. J. D. Brown and L. Parobek, X-ray Spectrometry 5 (19/6) 36.

16. R. Castaing and J. Deschamps, J. Phys. Radium 16 (1955) 304.

17. H. E. Bishop, Ph.D. Dissertation, University of Cambridge, 1966.

18. G. Shinoda, K. Murata and R. Shimizu, Quantitative Electron Probe Microanalysis, NBS Special Publication, No. 398 (1968) 155.

19. R. Shimizu, T. Ikuta and K. Murata, J. Appl. Phys 43 (1972) 4233.

20. D. F. Kyser, Introduction to Analytical Electron Microscopy, ed. J. J. Hren, J. I. Goldstein and D. C. Joy, New York, Plenum Press, 1979, 199.

21. S. Tolansky, Multiple Beam Interference Microscopy of Metals, London, Academic Press, 1970.

22. R. Glang, Handbook of Thin Film Technology, ed. L. I. Maissel and R. Glang, New York, McGraw Hill, 1970, 1-107.

23. K. L. Chopra, Thin Film Phoenomena, New York, McGraw Hill, 1969, 69.

24. D. E. Newbury, Private Communication, 1981.

25. G. W. Lorimer, Proc. EMAG 1981, Inst. Phys. Conf. Series, No. 61, 147.

26. N. Stenton, M. R. Notis, J. I. Goldstein and D. B. Williams, Quantitative Microanalysis with High Spatial Resolution. Conference Proceedings, UMIST, Manchester, March 1981, Metals Society, London, 35.

27. D. C. Joy, R. F. Egerton and D. M. Maher, SEM 1979, ed. O. Johari, Chicago, 817.

28. M. von Heimendahl and V. Willig, Norelco Reporter 27 (1980) 22.

29. G. Love, M. G. C. Cox and V. D. Scott, Developments in Electron Microscopy and Analysis 1977, ed. D. L. Misell, Bristol and London, The Institute of Physics, 1977, 347.

30. D. A. Rae, V. D. Scott and G. Love, Quantitative Microanalysis with High Spatial Resolution, Conference Proceedings, UMIST, Manchester, March 1981, Metals Society, London, 57.

31. J. Hillier and R. F. Baker, J. Appl. Phys. 15 (1944) 663.

32. D. C. Joy and D. M. Maher, Science 206 (1979) 162.

33. G. H. Curtis and J. Silcox, Rev. Sci. Instrum. 42 (1971) 630.

34. D. C. Joy, Introduction to Analytical Microscopy, eds. J. J. Hren, J. I. Goldstein and D. C. Joy, New York, Plenum Press, 1979, 223.

35. D. B. Williams and J. W. Edington, J. Microscopy 108 (1976) 113.

36. D. C. Joy and D. M. Maher, Proc. 35th Annual EMSA Meeting, 1977, 244.

37. R. F. Egerton and M. J. Whelan, J. Electron. Spectro. Rel. Phen. 3, (1974) 23.

38. R. F. Egerton, Phil. Mag 31 (1975) 199.

39. R. G. Menzies and R. H. Bricknell, Phil. Mag. 41 (1980) 493.

40. R. D. Leapman and V. E. Cosslett, Phil. Mag. 33 (1976) 1.

41. H. Bethe, Ann. Physik 5 (1930) 325.

42. R. D. Leapman, P. Rez and D. F. Mayers, J. Chem. Phys. 72 (1980) 1232.

43. D. C. Joy and D. M. Maher, Ultramicroscopy 5 (1980) 333.

44. R. P. T. Hills, R. P. Ferrier, R. D. Leapman and V. E. Cosslett, Proc. 7th Int. Conf. on X-ray Optics and Microanalysis, Moscow, 1974.

45. D. B. Wittry, R. P. Ferrier and V. E. Cosslett, J. Phys.(D). 2 (1969) 1767.

46. C. Colliex and B. Jouffrey, Phil. Mag. 25 (1972) 491.

47. D. C. Joy and D. M. Maher, J. Microscopy 124 (1981) 37.

48. R. F. Egerton, C. J. Rossouw and M. J. Whelan, Developments in Electron Microscopy and Analysis, ed. J. Venables, London, Academic Press, 1976, 129.

49. C. Colliex, V. E. Cosslett, R. D. Leapman and P. Trebbia, Ultramicroscopy 1 (1976) 30.

50. P. Trebbia and C. Colliex, Proc. 38th Annual EMSA Meeting, 1980.

51. N. J. Zaluzec, J. J. Hren and R. W. Carpenter, Proc. 38th Annual EMSA Meeting, 1980, 114.

52. M. Isaacson, SEM 1978, ed. O. Johari, Chicago, 763.

53. N. J. Zaluzec, Proc. 38th Annual EMSA Meeting, 1980, 112.

54. R. F. Egerton, Ultramicroscopy 4 (1979), 169.

55. R. F. Egerton, Proc. 39th Annual EMSA Meeting, 1981, 198.

56. F. L. Kennard, R. C. Bradt, and V. S. Stubican, J. Amer Ceram. Soc. 56 (1973) 566.

57. V. S. Stubican and J. R. Hellman, Science and Technology of Zirconia, Advances in Ceramics, Vol. 3, ed. A. H. Heuer, and L. W. Hobbs, American Ceramic Society, 1981, 25.

58. J. E. Wood, Private Communication, 1982.

59. J. I. Goldstein, Practical Scanning Electron Microscopy, eds. J. I. Goldstein and H. Yakowitz, Plenum Press, New York, 1975, 448.

60. Gatan Instruction Manual, Electron Energy Loss Spectrometer Model 607, Gatan Inc., Warrendale, PA, March 1981.

61. D. C. Joy, Private Communication, 1982.

62. R. E. Carter and W. L. Roth, Electromotive Force Measurements in High Temperature Systems, ed. C. B. Alcock, Inst. of Mining and Metallurgy, London, 1968, 125.

63. L. H. Schoenlein, L. W. Hobbs and A. H. Heuer, J. Appl. Crystallography, 13 (1980) 375.

64. J. G. Allpress and J. H. Rossell, J. Solid State Chem. 15 (1975) 68.

65. B. Hudson and P. T. Moseley, J. Solid State Chem. 19 (1976) 383.

66. J. B. Cohen, F. Faber and M. Morinaga, Science and Technology of Zirconia, Advances in Ceramics, Vol. 3, eds. A. H. Heuer and L. W. Hobbs, American Ceramic Society, 1981, 37.

67. H. J. Rossell, Ibid, 47.

68. S. P. Ray and V. S. Stubican, Mat. Res. Bull. 12 (1977) 549.

69. J. W. Edington, Practical Electron Microscopy in Materials Science, Van Nostrand Reinhold Company, New York, 1976, 153.

70. G. Remaut, R. Gevers, A. Lagasse and S. Amelinckx, Phys. Stat. Sol. 7 (1964) 497.

71. J. van Landuyt, R. Gevers and S. Amelinckx, Ibid. 13 (1966) 467.

72. R. Gevers, P. Delavignette, H. Blank and S. Amelinckx, Ibid. 5 (1964) 595.

73. R. F. Egerton, Ultramicroscopy, 3 (1978) 243.

APPENDIX I

Calculation of X-Ray Absorption

The Cliff-Lorimer equation can be used to determine concentrations providing there is no significant absorption of x-rays in the system of interest. If absorption is significant then it is necessary to apply a correction factor to the value of k_{AB} in order to obtain the true concentrations. The following correction factor has been proposed by Goldstein et al.[3] -

$$CF = \frac{\left.\frac{\mu}{\rho}\right]^{A}_{SPEC}}{\left.\frac{\mu}{\rho}\right]^{B}_{SPEC}} \left[\frac{1 - \exp\left(- \left.\frac{\mu}{\rho}\right]^{B}_{SPEC} \csc \alpha (\rho t)\right)}{1 - \exp\left(- \left.\frac{\mu}{\rho}\right]^{A}_{SPEC} \csc \alpha (\rho t)\right)} \right]$$

where ρ is the specimen density, t the foil thickness in cms, α is the x-ray take-off angle and $\mu/\rho]^{A}_{SPEC}$ is the mass absorption coefficient for x-rays of element A in the specimen. In a multi-component specimen $\mu/\rho]^{A}_{SPEC}$ is given by the following equation:

$$\left.\frac{\mu}{\rho}\right]^{A}_{SPEC} = \left.\frac{\mu}{\rho}\right]^{A}_{A} C_A + \left.\frac{\mu}{\rho}\right]^{A}_{B} C_B + \left.\frac{\mu}{\rho}\right]^{A}_{C} C_C \text{ etc.}$$

where C_A is the weight fraction of element A in the specimen.

Providing the absorption correction factor is ≤ 1.1 for any given foil thickness x-ray absorption may be considered negligible. Hence the absorption correction factor was determined for both phases of the eutectic assuming a foil thickness of 500 nm (which is thicker than most conventional TEM foils).

(a) $\underline{CaZrO_3}$

Ca wt. fraction $C_A = 0.224$

Zr wt. fraction $C_B = 0.509$

O wt. fraction $C_C = 0.268$

$$\left.\frac{\mu}{\rho}\right]_{spec}^{Zr_L} = 845.8 \times C_A + 700.9 \times C_B + 614.3 \times C_C$$

$$= 752.13$$

$$\left.\frac{\mu}{\rho}\right]_{spec}^{Ca_K} = 139.4 \times C_A + 1155.8 \times C_B + 115.8 \times C_C$$

$$= 650.56$$

$$CF = \frac{752.13}{650.56} \left[\frac{1-\exp(-650.56 \csc 20 (\rho t))}{1-\exp(-752.13 \csc 20 (\rho t))}\right]$$

$$\rho_{CaZrO_3} = 4.32 \text{ g/cm}^3$$

Assuming a foil thickness of 500 nm (5×10^{-5} cm)

$$CF = 1.156 \ \frac{1-(\exp - 8206.4 \times 5 \times 10^{-5})}{1-(\exp - 9487.7 \times 5 \times 10^{-5})}$$

$$CF = 1.0301$$

Absorption is negligible in $CaZrO_3$

(b) $ZrO_{2(ss)}$ (Assuming 20 mol % CaO)

Ca wt. fraction $C_A = 0.073$

Zr wt. fraction $C_B = 0.665$

O wt. fraction $C_C = 0.262$

$$\left.\frac{\mu}{\rho}\right]_{spec}^{Zr} = 700.9 \times C_A + 845.8 \times C_B + 614.3 \times C_C$$

$$= 774.57$$

$$\left.\frac{\mu}{\rho}\right]_{spec}^{Ca} = 139.4 \times C_A + 1155.8 \times C_B + 115.8 \times C_C$$

$$= 809.12$$

$$CF = \frac{809.12}{774.57} \quad \frac{1-\exp(-774.57 \csc 20 (\rho t))}{1-\exp(-809.12 \csc 20 (\rho t))}$$

$$\rho_{ZrO_{2(ss)}} = 5.35 \text{ g/cm}^3$$

Assuming a foil thickness of 500 nm.

$CF = 1.012$

<u>Absorption is negligible in $ZrO_{2(ss)}$</u>

APPENDIX II

Calculation of Beam Broadening

The beam broadening in a thin foil can be calculated using a single scattering model in which it is assumed that electron scattering occurs at the center of the foil. Goldstein et al.[3] have proposed the following equation for relating the beam broadening b to the operating voltage E_o and the foil thickness t:

$$b = 6.25 \times 10^5 \frac{Z}{E_o} \left(\frac{\rho}{A}\right)^{\frac{1}{2}} t^{3/2} \qquad (1)$$

where b and t are in cms; Z is the atomic number, A the atomic weight and ρ the density of the material and E_o is the accelerating voltage in eV.

When the foil is composed of more than one element the values of Z, A and ρ must be the weighted averages of each parameter.

(a) $CaZrO_3$

$$Z_{avg} = Z_{Ca} \times \text{wt.fraction Ca} + Z_{Zr} \times \text{wt.fraction Zr} + Z_o \times \text{wt.fraction O}$$

$$= 20 \times 0.223 + 40 \times 0.509 + 8 \times 0.268$$

$$= 26.96$$

$$A_{avg} = A_{Ca} \times \text{wt.fraction Ca} + A_{Zr} \times \text{wt.fraction Zr} + A_o \times \text{wt.fraction O}$$

$$= 40.08 \times 0.223 + 91.22 \times 0.509 + 16 \times 0.268$$

$$= 59.656$$

$$\rho_{avg} = \rho_{Ca} \times \text{wt.fraction Ca} + \rho_{Zr} \times \text{wt.fraction Zr} + \rho_{O} \times \text{wt.fraction O}$$

$$= 1.55 \times 0.223 + 6.49 \times 0.509 + 1.14 \times 0.268$$

$$= 3.954$$

Substituting in Equation (1)

$$b_{CaZrO_3} = 6.25 \times 10^5 \; \frac{26.96}{120 \times 10^3} \times \left(\frac{3.954}{59.66}\right)^{\frac{1}{2}} t^{3/2}$$

$$\underline{\underline{b_{CaZrO_3} = 36.15 \; t^{3/2}}}$$

i.e., For a foil thickness of 200 nm, b = 32.3 nm

(b) $\underline{ZrO}_{2(ss)}$ (Assuming 20 mol% CaO)

$Z_{avg} = 30.156$

$A_{avg} = 67.779$

$\rho_{avg} = 4.728$

Substituting in Equation (1)

$$\underline{\underline{b_{ZrO_{2(ss)}} = 41.48 \; t^{3/2}}}$$

i.e., For a foil thickness of 200 nm, b = 37.1 nm

APPENDIX III

Determination of Spectrometer Acceptance Angle β

The spectrometer acceptance angle β is a function of the objective aperture size. On the Philips EM400T there are three objective aperture sizes which may be selected, having diameters of either 20 μm, 50 μm or 100 μm. These diameters may be converted into a semi-angle β by means of a standard diffraction pattern, as outlined below:

(1) Obtain a low index diffraction pattern from a standard specimen, such as Al.

(2) Select one of the objective apertures and re-expose the plate to superimpose the image of the aperture on the diffraction pattern (Fig. 44).

(3) Index the diffraction pattern and calculate the semi-angle between a given set of planes using the following equation.

$$\lambda = 2\, d_{hk\ell} \sin\theta$$

At 120 kV $\lambda = 0.0335$

$d_{hk\ell}$ is obtained from tables.

e.g., For Al $\{220\}$

$$0.0335 = 2(2.025) \sin\theta$$

$$\sin\theta = 0.00827$$

For small angles $\sin\theta \simeq \theta$

$$\theta = 0.00827 \text{ rads}$$

$$2\theta = 16.54 \text{ mrads}$$

(4) Measure the interplanar spacing on the diffraction pattern corresponding to this angle.

e.g., For Al {220} the interplanar spacing is 12.75 mm

i.e., 12.75 mm corresponds to 16.54 mrads

(5) Measure the diameter of the objective aperture image on the diffraction pattern.

Relate this to an angle 2β using the conversion in (4)

e.g., The 20 μm objective aperture measures 3 mm on the image.

$$2\beta = \frac{3}{12.75} \times 16.54 \text{ mrads}$$

$$= 3.89 \text{ mrads}$$

$$\beta = 1.946 \text{ mrads for the 20 } \mu\text{m aperture.}$$

Since the relationship between aperture size and β is linear the other values of β corresponding to the 50 μm and 100 μm aperture sizes can be easily calculated.

VITA

Nicola Stenton was born to Betty and Robert Stenton on November 29, 1958, in Beverley, England. After attending various local schools, she completed her secondary education at Beverley High School with 3 A-levels and 9 O-levels. She obtained her Bachelor of Science in Materials Science, in the Faculty of Science at Manchester University, Manchester, England, in 1980, graduating with 1st Class Honors. Since this time she has been a graduate student in the Department of Metallurgy and Materials Engineering at Lehigh University.